Image Cover Sheet

CLASSIFICATION	SYSTEM NUMBER
UNCLASSIFIED	127305

TITLE

ANALYSIS AND TRIAL OF AN ACTIVE LONGWAVE INFRARED IMAGING SYSTEM FOR MINEFIELD DETECTION AND IDENTIFICATION

System Number:

Patron Number:

Requester:

Notes:

DSIS Use only:

Deliver to: JR

UNCLASSIFIED

DEFENCE RESEARCH ESTABLISHMENT SUFFIELD
RALSTON, ALBERTA

SUFFIELD REPORT NO. 576

ANALYSIS AND TRIAL OF AN ACTIVE LONGWAVE INFRARED IMAGING SYSTEM FOR MINEFIELD DETECTION AND IDENTIFICATION

by

Jean-R. Simard

UNCLASSIFIED

ABSTRACT

This document shows theoretical and experimental results of the capabilities of an active longwave infrared imaging system on surface-laid minefield. Three anti-tank and three anti-personnel mines on soil and prairie grass backgrounds are investigated for the detection and identification capabilities of this scanning imaging system. After establishing the detection and identification capabilities of the set-up used in this experiment, an associated parameter of the imaging system which can be used to estimate the detection and identification capabilities of other imaging set-ups with different configurations is evaluated. In addition, speckle is studied and its presence is demonstrated in the images obtained.

SOMMAIRE

Dans le present document, des resultats theoriques et experimentals presentant la capacite de former des images de mines de surface par un systeme d'imagerie actif utilisant l'infrarouge lointain sont rapportes. Trois mines anti-tanks et trois mines anti-personnels deposees sur sol terreux et sur les herbes des prairies sont etudies afin d'evaluer les capacites de detection et d'identification du systeme d'imagerie utilisant un scanner. Apres avoir etablis positivement la capacite de detection et d'identification du systeme utilise dans cet experience, on evalue un parametre associe au systeme utilise duquel d'autres systems possedant une configuration different peuvent etre compare. Cette comparaison aidera a estime les capacites de detection et d'idenfication de ces systemes projetes en fonction des resultats obtenus dans le present document. De plus, le bruit de speckle associe a un systeme d'imagerie utilisant un scanner est etudie et sa presence sur les images obtenues est presentees.

ACKNOWLEDGEMENT

The author would like to express his gratitude to Mr.Wayne Sirovyak for his work done to prepare the experimental set-up and his realisation of the software needed for the data acquisition involved in this experiment.

Table of Contents

List of Figures

List of Tables

List of Symbols

N.B. Constants between parentheses are the values associated to the symbols in this experiment and were used for the evaluation of expressions shown in this document.

BEM_i Mirrors used to perform Beam Expansion of the CO_2 laser.

SC SCanner.

CL Collecting Lens (f=10 cm).

D HgCdTe Detector.

CO_2 Carbon Dioxide laser.

HeNe Helium Neon laser used for optical alignment.

BS_1 20/80 (R/T) ZnSe sampling Beam Splitter.

BS_2 50/50 ZnSe Beam Splitter, responsible for the monostatic structure.

BS_3 80/20 ZnSe sampling Beam Splitter.

M_i Flat Mirrors.

FM Focusing Mirror (f=30 cm) for the spectrum analyser (S).

TA Target Area.

EO Electro-Optic modulator.

P IR Polarizer.

PM Power Meter.

SA Spectrum Analyser.

W Ge anti-reflection Window to introduce the HeNe laser along the CO_2 beam path.

BD Beam Dumping system to minimize the split CO_2 beam return.

S Opaque Screen.

o Point where the optical axis intercepts the target plane.

R Total distance between the screen and the starting position of the Gaussian beam.

AS Aperture Stop.

FS Field Stop.

$\left(\frac{S}{N}\right)_c$ Current Signal-to-Noise ratio.

Δf Frequency band.

ϕ_D Detector diameter.

ϕ_{CF} Contour Field diameter.

ϕ_{PCF} Partial Contour Field diameter.

ϕ_o Minimum Gaussian beam diameter.

ϕ_1 Initial Gaussian beam diameter.

ϕ_2 Gaussian beam diameter at the screen.

ϕ_z Gaussian beam diameter along the trajectory.

z Coordinate along the trajectory from the position of the minimum diameter ϕ_o.

z_1 Distance along the trajectory between the position of ϕ_o and the initial position.

z_2 Distance along the trajectory between the position of ϕ_o and the scanned screen.

$\Delta\varphi$ Total scanned angle.

d_{FS-TA} Distance from Field Stop to Target Area.

d_{AS-FS} Distance from Aperture Stop to Field Stop.

d_{AS-TA} Distance between Aperture Stop and Target Area ($d_{AS-TA} = 37.5$ m).

$\Re$ Overall Responsivity (4.5 A/W).

$\Delta\rho$ Contrast reflectivity.

ξ Hemispherical blackbody emissivity ($1/\pi$).

$\mathbf{P_L}$ Averaged Lasing Power (3 W).

$t_{\mathrm{L-TA}}$ Overall transmission of optical components from Laser to Target Area (0.13).

t_{A}^2 Optical Atmospheric transmission (1.0).

$t_{\mathrm{TA-D}}$ Overall transmission of optical components from Target Area to Detector (0.24).

$\mathbf{A_{AS}}$ Aperture Stop Area ($\pi \left(\frac{\phi_{\mathrm{AS}}}{2}\right)^2 = 0.0013\ \mathrm{m}^2$).

η Field of view matching factor (0.85).

$\mathbf{A_T}$ Radiating Area sees by the Detector ($\left(\frac{.2\mathrm{mm} \times .2\mathrm{mm}}{\mathrm{f}}\right)^2 = 0.0056\ \mathrm{m}^2$).

$\mathbf{M}^{\mathrm{B}}_{10.6,.35}$ Blackbody irradiance for a .35 μm wavelength bandwidth center at 10.6 μm (11 $\mathrm{W/m^3}$).

NEP Noise Equivalent Power ($6.7 \times 10^{-13}\mathrm{W}/\sqrt{\mathrm{Hz}}$).

$\mathbf{M}^{\mathrm{B}}_{\lambda}$ Spectral radiant exitance or Blackbody power spectral density distribution emitted by unit surface for a particular wavelength and temperature.

e Electronic charge (1.6×10^{-19} C).

λ Wavelength (10.6 μm).

T Temperature (300°K).

ν Electromagnetic frequency (c/λ).

h Planck constant (6.62×10^{-34} J-s).

k Boltzmann constant ($1.38 \times 10^{-23}\mathrm{J/°K}$).

c Speed of light (3×10^8 m/s).

1. Introduction

Among the subjects currently being studied by the Threat Detection Group (TDG) at DRES is the detection of surface laid land mines. One potentially useful method to detect and locate these mines is the use of an active infrared imaging system.

In this document, a presentation is given of experimental images of land mines obtained in a simulated exterior minefield using an active infrared imaging system working at 10.6 μm. The active infrared imaging system comprises a CO_2 waveguide laser, a HgCdTe detector and a 2-D scanner. To simulate a vertical point of view to the minefield, a 15 meter high tower is used. In addition, a system of mirrors carries the laser beam from a ground station to the top of the tower before being redirected vertically to the minefield. Symmetrically, the reflected signal from the minefield will follow counter-directionally the path of the laser back to the ground station where the signal is processed. The complete trajectory simulates a view point which is 40 meters vertically above the simulated minefield.

To describe and analyse this experimental trial, the first chapter will present a complete description of the experimental set-up. Optical, radiometric and noise characterizations will be stated and used to fully describe the set-up. From this characterization, a model for the resolution and signal-to-noise ratio is deduced.

The active IR images of the minefield are shown in Chapter 3. Six types of mines are studied: TMN-46, PM-60, TMB-D (anti-tank mines), and PMN-6, OZM-3, PFM-1 (anti-personnel mines). A qualitative description of the detection and identification capabilities is given. Chapter 4 presents a more quantitative analysis of the images produced. The imaging resolution is evaluated and speckle noise effects are analysed and discussed. Most important, the signal-to-noise ratio associated with this experimental imaging system for mine detection and identification is evaluated using the model developed in Chapter 2. From this model and the results introduced here, extrapolation rules are stated to transpose the detection and identification capabilities of this set-up to others with different configurations.

2. Description of the Experimental Set-Up

2.1 Structure of the Experimental Set-Up

To simulate an airborne active long-wave (10.6 μm) IR mines imaging system, a stationary tower was used (Figure 2.1). This tower allowed a simulation of a 40 meter high imaging system with a nearly vertical point of view. This configuration is closely comparable to the projected imaging system installed in a flying carrier except that the later is at a higher altitude (150 meters is the probable maximum height), but extrapolation can be made as described in section 4.2. Table I shows the important distances involved in the experimental set-up. The active imaging configuration used in this experiment possesses two basic characteristics. First, it uses a direct detection optical design. Direct detection is obtained when the reflected laser illumination intensity from the target area is directly transformed in signal current with the help of a photodetector. Second, the optical set-up follows a monostatic configuration. In this, the illuminating laser beam and the reflected signal to be detected travel counter-directionally along the same trajectory. More specifically, this experimental set-up is composed of three main sections: the shelter, the tower, and the target area as shown in Figure 2.2 [1]. The majority of the optics is located in the shelter. This is where the illumination source is located and where the detection process is performed. The scanning components are installed at the top of the tower. The target area, situated at the foot of the tower, is the site where mines and backgrounds are scanned by the imaging system. A number of mirrors carry the laser beam between each of these sections. The following text will describe this experimental set-up in more detail.

Most of the sensitive components used in this experiment are confined in the shelter. This is where the illuminating source is located. This source is a CO_2 waveguide laser and its characteristics are described in Table II. Because of the detection method implied in this experiment, the illuminating laser beam is amplitude modulated. This detection technique, using a phase-lock amplifier, will be described in Section 2.3. The amplitude modulation of the laser is created by an electro-optic

[1] The label identifiers in this figure are described in the list of symbols.

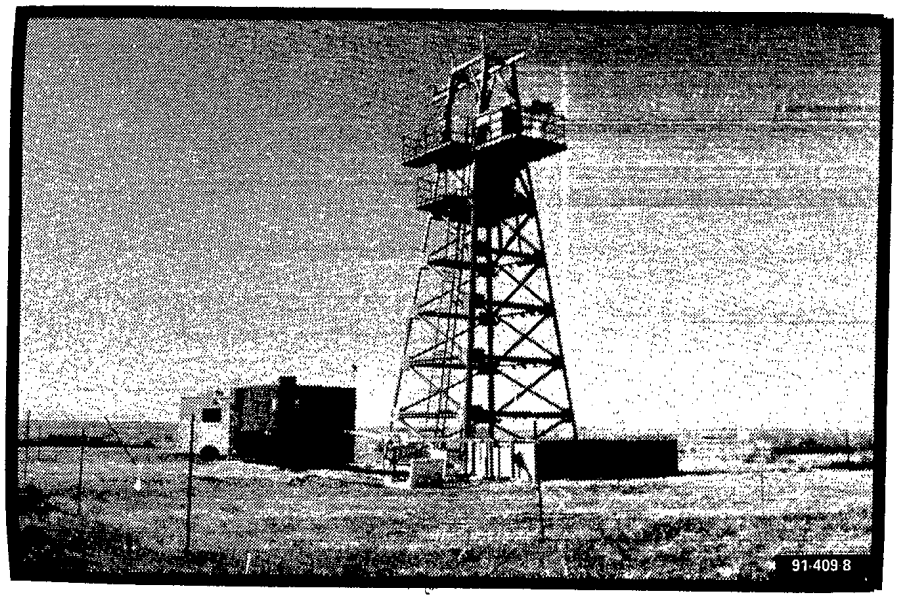

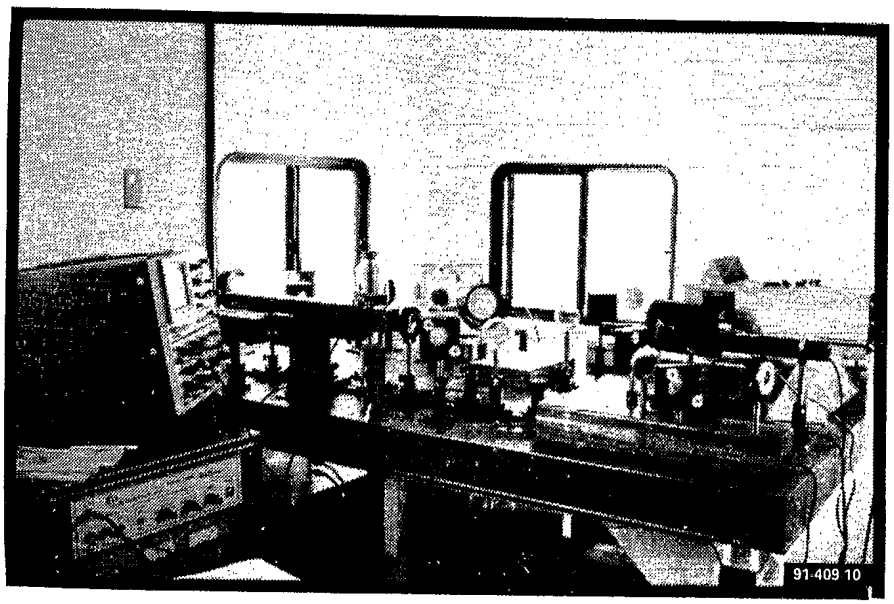

Figure 2.1

Experimental set-up. The upper picture shows the shelter (in blue), the tower, and the target area (surrounded by the wooden fence), the lower picture shows a view of the optical set-up inside the shelter.

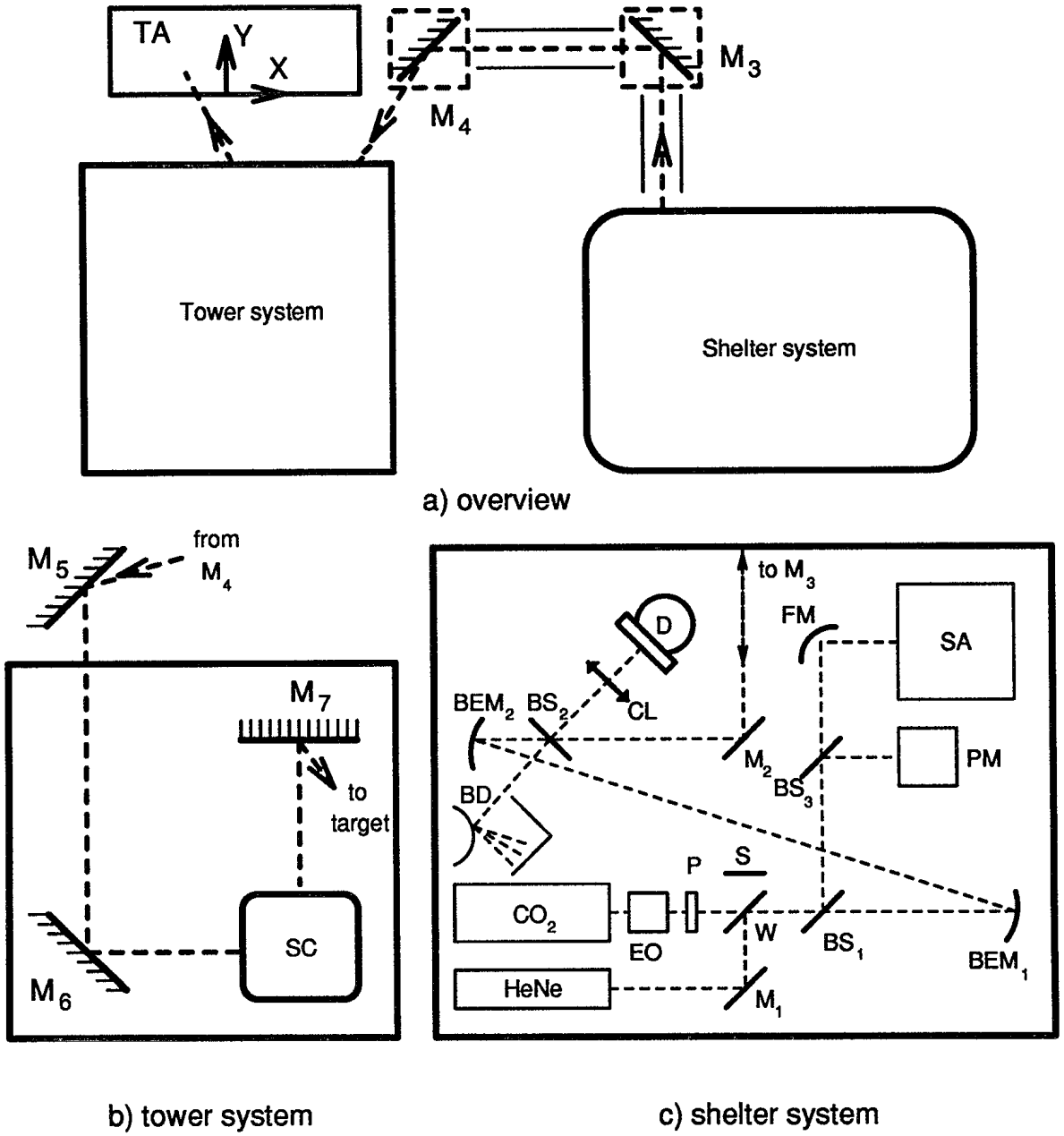

Figure 2.2

Schematic view of the experiment set-up: a) overview, b) optical set-up on the tower, c) optical set-up in the shelter. Symbols are described in the list of symbols.

modulator (EO). This electro-optic modulator, described in Table III, rotates the polarization state of the laser beam when an electric voltage is applied. By positioning a polarizer after this electro-optic modulator, it is then possible to modulate the intensity of the laser beam. To obtain the amplitude modulation, 3 KV at a frequency of 100 KHz was applied to the EO. To monitor the total laser power and lasing wavelength during image acquisition, a 20/80 (reflected intensity/transmited intensity) ZnSe beam splitter (BS_1) samples the laser beam and redirects it to a power meter (PM) and a spectrum analyser (S). Next, the laser beam is expanded with two concave mirrors (BEM_1 and BEM_2). These two mirrors, with focal lengths of 25 and 100 cm respectively, give a 4X beam magnification. The long focal length chosen for these mirrors allows the reduction of the laser beam distortion caused by off-axis reflection (comatic aberration). The second beamsplitter (BS_2), a 50/50 ZnSe window, is the main component achieving the monostatic structure of the whole set-up. The illuminating beam passing through this window, after losing 50% of its intensity in reflection, illuminates the target area. Then, the detected light produced by the reflection of this illuminating beam at the target area follows the same trajectory in the counter-direction and is reflected back by the same beam splitter (BS_2) to the detector (D) after being integrated by the collecting lens (CL). The detector is a HgCdTe photovoltaic detector cooled to 77°K. A description of this detector is given in Table IV, which can be found in section 2.3. In order to eliminate all interference of the illuminating beam reflected during the first pass at BS_2, this reflected light is directed to a beam dumping system formed by a short focal convex mirror and a high absorption screen. This system minimizes the return to the detector from this part of the reflected illuminating beam. A powerful Helium-Neon laser (HeNe) is aligned with the CO_2 laser to facilitate the positioning of all the optical components inside and outside the shelter, and to facilitate the location of the scanning beam at the target area.

To carry the illuminating beam and the return signal between the shelter and the tower, two large mirrors (M_3 and M_4) were installed on ground supports with positions showed in Figure 2.2 a). These mirrors were enclosed in plexiglass boxes and PVC tubes are placed along the laser beam trajectories to ensure a good confinement of the IR laser light.

The tower optical system is essentially composed of mirrors and the scanner. A first mirror (M_5) receives the beam from the ground mirror (M_4) and it is directed to the scanner (SC). A last mirror (M_7) reflects the scanning beam in a vertical direction to the target area. The path followed by the scanning beam at the target area is showed in Figure 2.3. The area vertically under the last mirror (M_7) is located at the bottom center of the scanned area (point (0,0)). The scanning angle covers $\pm 9.7°$ in the X direction and from 0° to +9.7° in the Y direction (the positive Y direction points away from the tower's foot), which corresponds to a scanned area of 4.8 m X 2.4 m. To facilitate the identification of an IR image, four unpolished

Table I

Important Dimensions of the Experimental Set-Up.

Total Laser Path Length		39.5 m
Inside Shelter	3.8 m	
Shelter to M_3	3.6 m	
M_3 to M_4	3.5 m	
M_4 to M_5	14.1 m	
M_5 to M_7	1 m	
M_7 to Target Area	13.5 m	
Mirrors Clear Diameter (min)		75 mm
Beam Splitter Clear Diameter (ϕ_{BS_1})		40 mm
Collecting Lens Clear Diameter (ϕ_{CL})		45 mm
Scanner Clear Diameter (ϕ_{SC})		27 mm
Distance CO_2 Laser to BEM_1 ($d_{CO_2-BEM_1}$)		71 cm

Table II

Characteristics of the CO_2 Waveguide Laser.

Type	Waveguide
Manufacturer	Laser Photonics
Model	CL-75
Dimension	3.8 in. X 3.1 in X 18.5 in (17 lbs)
Power	7 Watts
Wavelength	10.6 μm
Beam Divergence (θ_{CO_2})	8 mrad

Table III

Characteristics of the Electro-Optic Modulator and its Pulse Generator.

Electro-Optic Modulator		Pulse Generator	
Materiel	CdTe	Manufacturer	II-IV Inc.
Manufacturer	II-IV Inc.	Model	HVPG-362-E
Model	EOM3-10.6-0350-C	Frequency	1 Hz to 200 KHz
Dimension	3mm X 3 mm X 50mm	Voltage	0 to 3 KV
$V_{\lambda/2}$	3200 Volts	Current	0 to 40 mA

aluminium discs have been placed at corners of the scanned area. In order to control the image acquisition process, an optical fibre system links the scanner controller to a 386 IBM PC computer installed in the shelter. This connection allows scanning control and makes possible to relate the reflected signal detected and stored by the computer to a particular point of the scanned area.

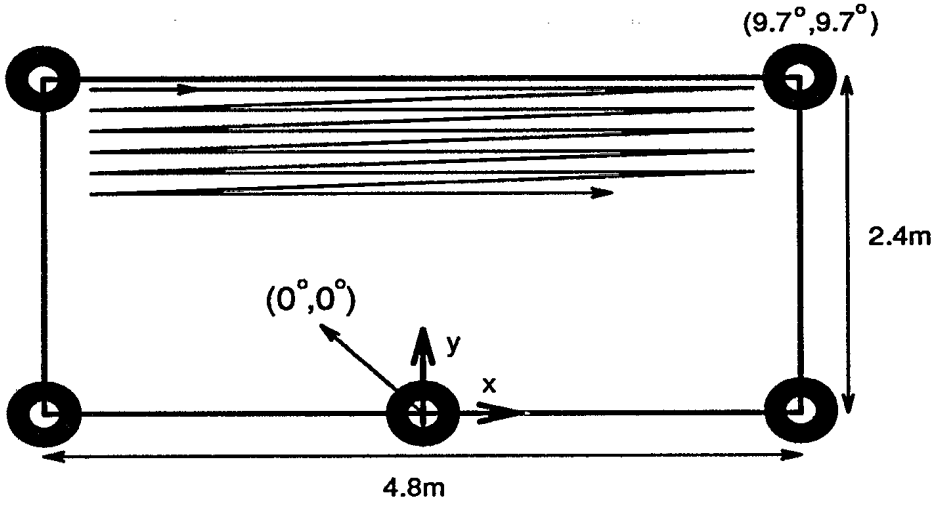

Figure 2.3

Scanning scheme. The scanning process begins at the upper left corner and scans from left to right in a raster pattern. Five unpolished disks delimit the scanned area.

Two different background types and six different replica mines were placed in the target area to obtain active IR images. Soil and prairie grass as backgrounds were used along with the following replica mines: PM-60, TMN-46, TMB-D, PMN-6, OZM-3 and PFM-1; all replica mines were Russian made. The three first ones are anti-tank and the last three are anti-personnel. Appendix D shows photographs of these mines; more technical information on the replica mines is available in [1].

The detection process scheme is illustrated in Figure 2.4. The different stages of detection proceed as follows. First, the signal coming back from the target area is quantified by the HgCdTe photovoltaic detector after being reflected by the BS_2 and spatially integrated by the collecting lens (CL). Next, the modulated electrical signal coming out of the detector is preamplified. This first stage of amplification fixes the electronic signal-to-noise ratio (S/N). Third, a lock-in amplifier demodulates the signal and amplifies it to an adequate voltage level for the analogue/digital (A/D) converter. The use of this type of amplifier reveals three major advantages: high quality customized gain, narrow equivalent bandwidth, and demodulated background signal reduction. Following the amplification stages, the output voltage signal is digitized with a 12 bit A/D converter. Then, the digitized data are stored on the computer hard disk and linked to the area illuminated via the scanning control. For

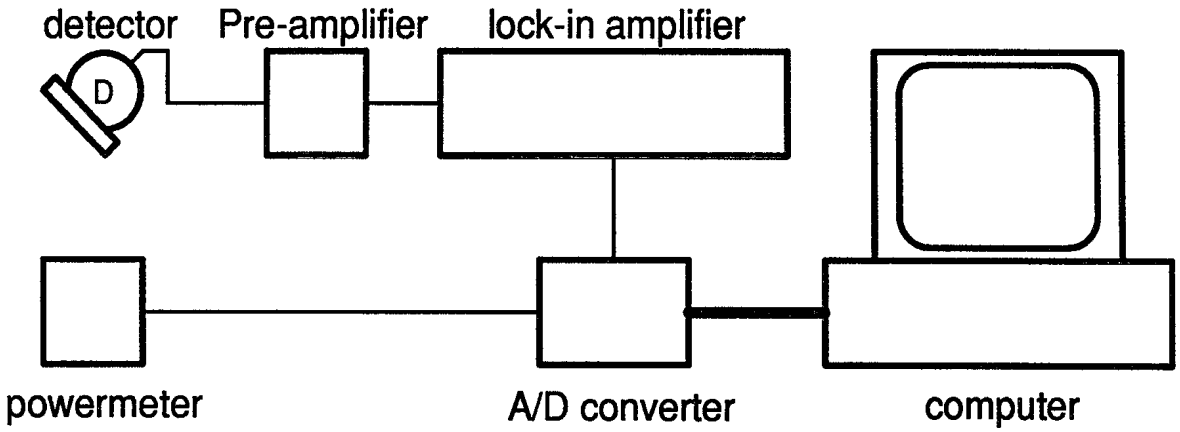

Figure 2.4

Scheme of the detection system and storage of the reflected signal.

each of these conversions from the output of the lock-in amplifier, a reading of the power meter (PM) is digitized and stored to allow the pixel values of the image to be corrected for variations in laser output power. The final image can then be further analyzed for contrast, S/N ratio, identification, and false color image reconstruction. These operations on IR images will be shown in Chapter 3. A more complete and detailed description of the detection process will be introduced in section 2.3.

2.2 Imaging System Resolution and Radiometric Considerations

For this experimental set-up, two aspects of the optical arrangements have to be analysed to optimize the imaging system [2]. These are the resolution of the laser beam illuminating the target area and the amount of reflected radiation received by the detection system. As will be seen below, the resolution of the imaging system depends essentially on two components: the laser beam spot size at the target area and the product of the electronic integration time of the detection process and the scanning speed. Next, to evaluate the amount of signal measured by the detection system, radiometric considerations have to be analysed. Equations will be introduced to model adequately the optical system formed with the scanner, mirrors, beam splitters, collecting lens, and detector to quantify the level of signal received by the detector. This analysis is shown in subsection 2.2.2.

2.2.1 Evaluation of the Imaging System Resolution

As mentioned previously, to establish if the illumination function of the laser is correctly performed in this imaging system, the resolution achieved by the scanning laser beam and the laser beam efficiency to illuminate the target area without substantial losses are evaluated. The resolution determined by the scanned laser beam depends on two characteristics of the experimental set-up: the laser beam spot size at the target area and the integration time of the detection system multiplied by the scanning speed. The resolution associated with the laser spot size, for this experiment, has been chosen arbitrarily to be the diameter of the laser spot at $1/e^2$ of its intensity at the target area. This decision was based on two features of the laser spot: the Gaussian characteristic of a laser beam (see appendices A and B) and the 63% modulation of the reflected light when a reflection grating of period equal to the laser beam diameter (ϕ_{1/e^2}) is scanned [3]. Following this choice, the distance between adjacent scan lines was adjusted to this particular distance (ϕ_{1/e^2}). In this direction (direction Y in Figure 2.3), the integration time associated to the detection has no effect and the resolution is essentially defined by the laser spot dimension. The resolution of the imaging system in the X direction does not only depend of the laser beam spot size at the target area but also on the spot displacement during the electric signal detection integration time. This fact results from the scanning aspect of the laser beam illumination technique used. To register a change of reflectivity, the detection system needs some time to react. To evaluate the response time result-

[2]The descriptive theory shown here is based on material from [2] and [3].

[3]Analysing the modulation associated to the scan of a reflectivity grating is equivalent to an analysis based on single point resolution. The first method implies the frequency domain while the second is done in the time domain; however each method produced the same result in the evaluation of the resolution limit of an imaging system.

ing from the signal integration ($\tau_{1/2}$), we will use the time needed for the signal to decrease to half of the initial voltage after switching to zero the input voltage (fall time). Using this time response with the scanning speed (SS) (which is the travelling speed (m/s) of the laser spot at the target area during the scanning process), and the laser beam spot size (ϕ_{1/e^2}), it is possible to define an approximate theoretical resolution of the imaging system as follows.

$$\Delta Y = \phi_{1/e^2} \tag{2.1}$$
$$\Delta X = \phi_{1/e^2} + 2 \times \tau_{1/2} \times \mathrm{SS} \tag{2.2}$$

The factor 2 introduced comes from the rise and fall time associated with the electric signal time constant. In this experiment, the corresponding signal integration distance of the detection electronics of ($2 \times \tau_{1/2} \times$SS) was kept at 4 cm for most of the IR images shown here. Thus if one uses $\tau_{1/2} = 3$ ms to make an image, it is inferred that the SS associated to this time constant is 3 times slower than the one associated with 1 ms, keeping the product $2 \times \tau_{1/2} \times$SS= 4 cm.

The optimum optical resolution expected in a scanning system as the one presented in this report depends on the diameter of the laser beam after the beam expansion process ($\phi_{\mathrm{BEM_2}}$) and the distance from this location to the target area ($d_{\mathrm{BEM_2-TA}}$). As described in appendices A and B, the minimum spot size achieved theoretically is fixed by the relation

$$\phi_{1/e^2}^{\mathrm{min}} = \frac{4\lambda d_{\mathrm{BEM_2-TA}}}{\pi \phi_{\mathrm{BEM_2}}} \tag{2.3}$$

$d_{\mathrm{BEM_2-TA}}$ can be evaluated using the distance given in Table I as 37.5 m. $\phi_{\mathrm{BEM_2}}$ is calculated from the magnification of the beam expansion process (4X), the divergence of the CO_2 laser ($\theta_{\mathrm{CO_2}}$), and the distance between the CO_2 laser and $\mathrm{BEM_1}$ ($d_{\mathrm{CO_2-BEM_1}}$)

$$\phi_{\mathrm{BEM_2}} = 4 \times 2 \times d_{\mathrm{CO_2-BEM_1}} \times \tan \frac{\theta_{\mathrm{CO_2}}}{2} \tag{2.4}$$

In this expression, $\theta_{\mathrm{CO_2}}$ is given in Table II as 8 mrad; $d_{\mathrm{CO_2-BEM_1}}$ is given in Table I as 71 cm. From those values, $\phi_{\mathrm{BEM_2}}$ is evaluated as 2.27 cm. Using this last parameter and the value of $d_{\mathrm{BEM_2-TA}}$ in relation 2.3, the laser beam spot size is

$$\phi_{1/e^2}^{min} = 2.23 \ \mathrm{cm} \tag{2.5}$$

Figure 2.5 shows how the minimum laser spot size at the target (ϕ_{1/e^2}^{min}) is a function of the initial laser beam diameter ($\phi_{\mathrm{BEM_2}}$) for $d_{\mathrm{BEM_2-TA}}$ involved in this experimental set-up.

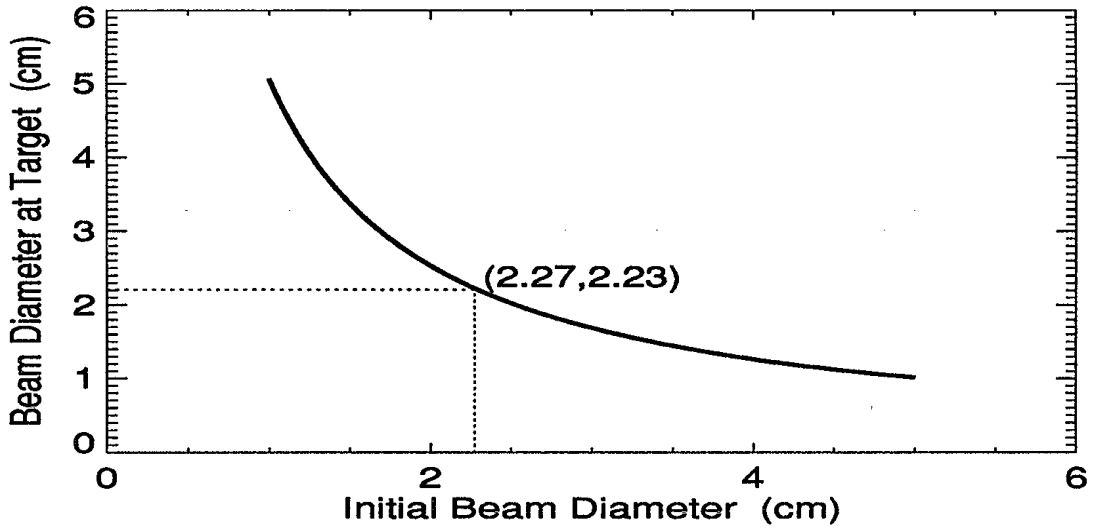

Figure 2.5

Minimum laser beam size at the target area ($\phi_{1/e^2}^{\min}$) as a function of the initial laser beam diameter (after BEM_2) for the distance BEM_2 (d_{BEM_2-TA} = 37.5 m). This graph is obtained using equation 2.3.

ϕ_{1/e^2} is also an important parameter to ensure that most of the energy carried by the laser reaches the target area without being blocked by optical components having too small apertures. As demonstrated in appendix A, an optical aperture having a diameter equal to the laser beam diameter at $1/e^2$ will let pass 87% of the total laser power. This dimension is important because an optical component with an aperture approaching this minimal dimension will significantly perturb the Gaussian profile and increase the diffraction effect on the laser beam, which will reduce the optical resolution. Figure 2.6 shows, for the conditions described previously, the $1/e^2$ diameter of the laser beam along the laser beam path from BEM_2 to the target area. The laser beam travels across the optical components of the optical set-up without being screened, as seen in this figure, when the laser is precisely aligned.

2.2.2 Radiometric Considerations

As mentioned in the introduction of this section, a radiometric analysis has to be performed to evaluate the amount of reflected light received by the detector. This is essentially asking what part of the target area is seen through the optical set-up by the detector, and what quantity of this reflected light is collected to form the image of the target area. This analysis will give information on the amount of the illuminating laser spot, which is reflected, contributes to form the signal at the detector. It will also give information on the area surrounding the laser spot seen by the detector. In

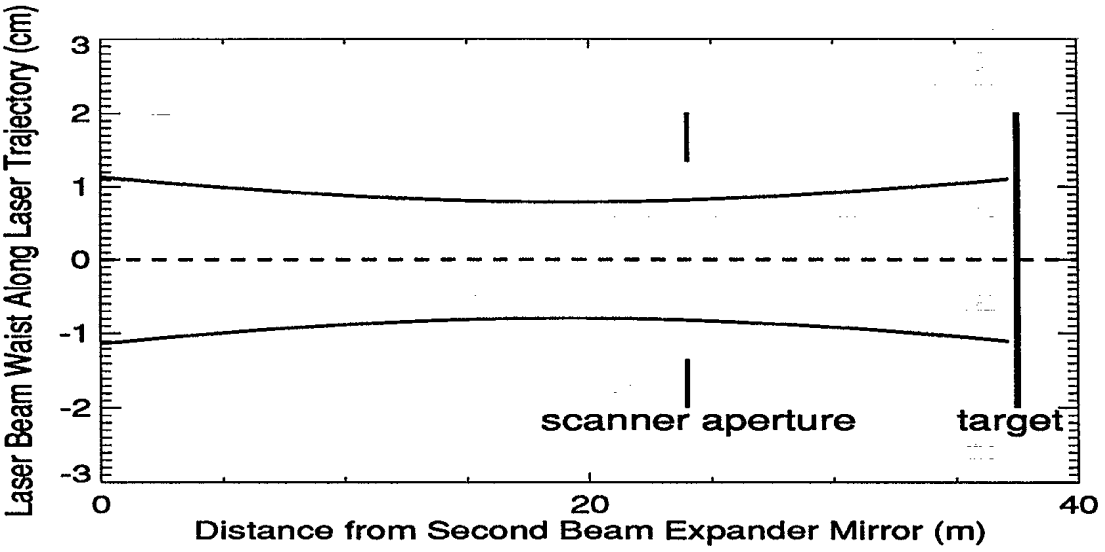

Figure 2.6

Laser beam shape between the shelter and the target area. The scanner aperture is shown at its position along the beam trajectory.

an active IR imaging system like the one described here, one wants to keep the area seen by the detector surrounding the laser spot as small as possible to keep a low background signal. In a airborne active IR imaging system, to achieve this condition, one simply adjusts the field of view of the detector to the laser beam divergence. But in this experimental set-up, because many optical components are placed along the laser trajectory, a more complete radiometric analysis will have to be performed. To do so, the following radiometric parameters: aperture stop, field stop, contour field and partial contour field will be defined and evaluated.

All optical imaging systems reproduce a spatial intensity distribution of a real object. In this case, the real object is a portion of the target area. The optical system is composed of the detector, the collecting lens, BS_2, M_2 to M_7, and the scanner. The surface of the target area seen be the optical system can be considered as a multitude of point sources, each of them radiating uniformly in the direction of observation with its own intensity. The optical system will pick up only part of their total radiated intensity. Especially inside the contour field (which will be defined later), this fraction is the same for each point of the object. This collected radiation forms a cone whose tip is the point source and whose base is a particular optical component of the imaging system. The size of this optical component will limit the amount of irradiated light getting in the imaging system. This particular optical component is called the aperture stop. Because an imaging system uses only part of the incoming light, it will always be possible to identify one and only one aperture stop in an imaging system. The larger this aperture stop, the larger will be the amount of

light collected and the signal detected. The aperture stop thus forms a basic element describing an optical system. As most imaging systems are formed with at least two components, the simplest one being a lens or a mirror with a detector, there will be always another optical component which restricts an imaging system from receiving the radiated light from the whole object plane. This second component will fix the region of the target area seen by the detector. This particular component is called the field stop. Like the aperture stop, there is only one field stop for an imaging system. Those two components can be considered as forming a tube where only particular rays can pass through each of its ends. These two components, the aperture stop and the field stop, are the basic parameters describing the geometric organization of an imaging system. The amount of light coming from the object can be quantified (specifying the signal level) by the aperture stop and the field of view of the imaging system is fixed by the field stop. In the following text, it will be shown that the aperture stop and the field stop can be identified for any imaging system and that this technique can be applied to the experimental set-up shown in Figure 2.2. Figure 2.7 shows a scheme of the radiometric structure of this experimental set-up. This scheme represents the complete set-up with all mirrors and other optical components along the laser beam trajectory but only the field stop and the aperture stop are shown. In fact, when these two components are identified, all other components can be neglected. The different terms and symbols are defined in the list of symbols and in the following text. In this analysis, a perfect optical alignment is assumed.

Aperture Stop (AS) Identification

The aperture stop is the optical component of the imaging system that restricts the irradiated light cone coming from a point source at the target plane. To identify it, the optical component introducing the smallest solid angle seen from the point source placed at the interception of the optical axis and the target plane is determined. This point is identified as "o" in Figure 2.7. The aperture stop can be defined as the optical component having the smallest value for the expression $\frac{\phi_{OC}}{d_{OC-TA}}$, where ϕ_{OC} is the diameter of an optical component and d_{OC-TA} is the distance between this optical component and the target plane. By applying this definition to the imaging system presented in Figure 2.2, and comparing the above for all the optical components, the **Beam Splitter 2 (BS_2)** is found to be the component having the smallest solid angle see from the point "o". For this component $\phi_{BS_2} = 40$ mm and $d_{BS_2-TA} \simeq 37.5$ meters.

Field Stop (FS) Identification

In a similar fashion, the method to identify the field stop is described. As discussed previously, the field stop is the optical component of the imaging system that restricts the field of view. The field stop is the optical component which will most restrict the

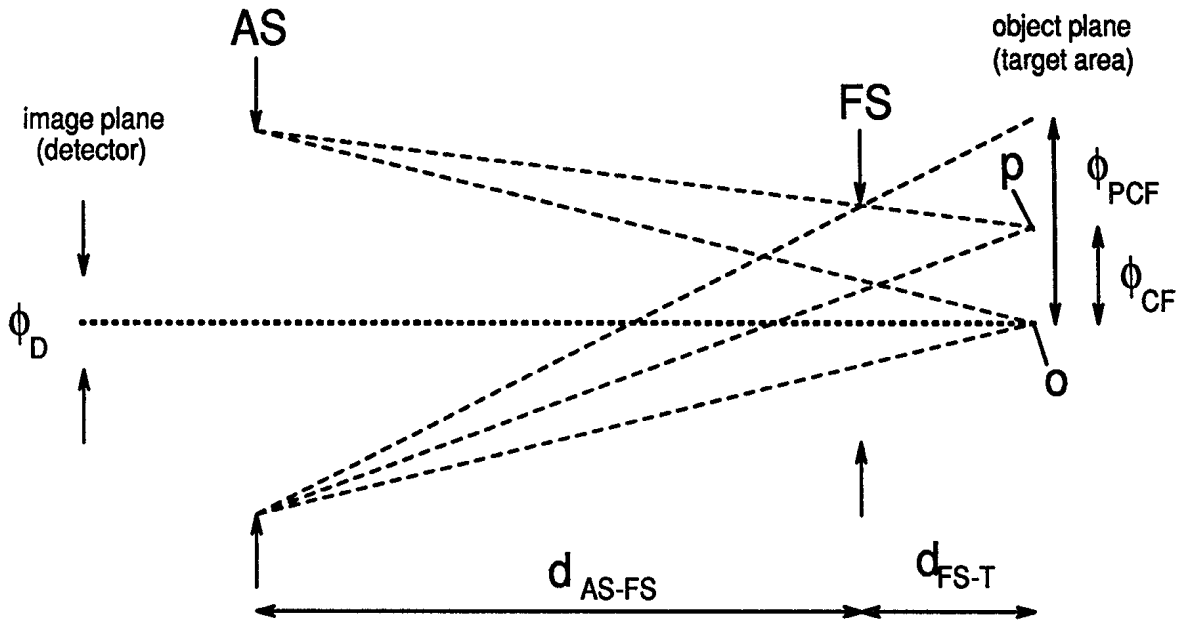

Figure 2.7

Schematic view of the geometry of the optical set-up. It will be used to evaluate the aperture stop, the field stop, the contour field and the partial contour field. Symbols are described in the list of symbols.

incoming light from a point source at the object plane from covering the aperture stop completely(see point P in Figure 2.7). It is possible to quantify this condition by finding the optical component having the largest value for the expression $\frac{\phi_{AS}-\phi_{OC}}{d_{AS-OC}}$, where ϕ_{AS} is the diameter of the aperture stop found previously, and d_{AS-OC} is the distance between the aperture stop and the optical component in question. When this expression for the experimental set-up is evaluated using the parameters gave in Table I, the **scanner (SC)** is identified to be the field stop with $\phi_{SC} = 27$ mm and $d_{AS-SC} \simeq 24$ meters.

Evaluation of the Field of View

When the aperture stop and the field stop are identified, the region of the target plane as seen by the imaging system can be evaluated. This field of view is separated in two components: **the contour field (CF)** and **the partial contour field (PCF)**. The contour field is the region of the object plane where point sources of the object plane cover the aperture stop totally with their irradiation. The partial contour field is the region surrounding the contour field from which irradiated light covers the aperture stop only partially. Therefore, the contour field will appear with the true intensity distribution while the partial contour field will appear darker as one goes from the CF limit to the PCF limit. The dimension of the contour field and the partial contour field is evaluated with the next two relations:

$$\phi_{CF} = \phi_{FS} - \frac{d_{FS-TA}}{d_{AS-FS}}(\phi_{AS} - \phi_{FS}) \quad (2.6)$$

$$\phi_{PCF} = \phi_{FS} + \frac{d_{FS-TA}}{d_{AS-FS}}(\phi_{AS} + \phi_{FS}) \quad (2.7)$$

From outside the region defined by ϕ_{PCF}, the incoming light passing through the FS will not reach the aperture stop and thus will not be seen by the detector.

For this experiment, the important radiation coming from the point sources is the reflected part of the laser beam. It is then preferable that the laser beam size at the target area be smaller than the CF. By using the diameter and distance found previously for the aperture stop and the field stop for our imaging system ($\phi_{AS} = \phi_{BS_2} = 40$ mm, $\phi_{FS} = \phi_{SC} = 27$ mm, $d_{FS-TA} \simeq 14$ m and $d_{AS-FS} \simeq 24$ m), from these two relations (2.6 and 2.7), ϕ_{CF} and ϕ_{PCF} is evaluated as

$$\phi_{CF} = 1.9 \quad \text{cm} \quad (2.8)$$

$$\phi_{PCF} = 6.6 \quad \text{cm} \quad (2.9)$$

By comparing ϕ_{CF} to the minimum diameter of the laser spot in the target area ($\phi^{min}_{1/e^2} = 2.23$ cm), it is appeared that most of the laser illumination is in the contour field area but part of it will fall in the partial contour field. This fact will have to be taken in account in the section on signal detection (section 2.3).

Detector Size (ϕ_d) Consideration

There is one last point to examine in order to analyse the radiometry of the imaging system used in our experiment. This is to ensure that all laser reflected irradiation coming from the contour field and the partial contour field reach the detector to be transformed in electric signal. In other words, to ensure that the image of the PCF made by the collecting lens in the detection plane is smaller than or equal to the detector size. Because the distance from the collecting lens to the target area (d_{CL-TA}) is much greater than the distance from the collecting lens to the detector (d_{CL-D}), the distance lens-detector can be assumed to be approximately equal to the focal length of the lens used ($d_{CL-D} \simeq f$). The dimension of the image of the PCF made by the collecting lens is given by one of two different expressions depending on whether or not the diffraction-limited imaging mode is applicable. These two modes of imaging can be expressed numerically by the next two equations

$$\phi_{diff} = \frac{1.22\lambda}{\sin\left(\arctan\frac{\phi_{AS}}{2f}\right)} \quad (2.10)$$

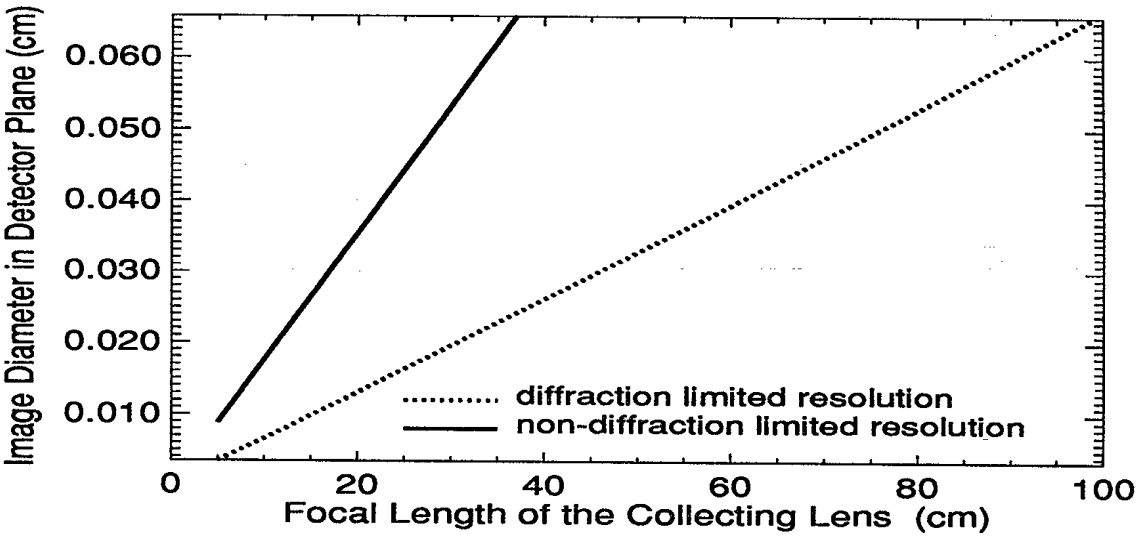

Figure 2.8

The diameter of the PCF image in the detector plane as a function of the focal length of the collecting lens in two different situations (normal and diffraction-limited imaging) for the case of the tower experiment.

$$\phi_{ima} = \frac{f}{d_{\text{CL-TA}}}\phi_{\text{PCF}} \qquad (2.11)$$

Figure 2.8 shows the diameter of the image of the PCF in the detector plane depending on the imaging mode used as a function of the focal length of the collecting lens. In this analysis ϕ_{AS} is used because the effective diameter of the collecting lens is the diameter of the aperture stop (BS_2). The right model describing the image of the PCF in the detector plane for the present set-up is the one giving the larger diameter for the conditions involved. From Figure 2.8, with $\phi_{\text{PCF}} = 6.6$ cm, the non-diffraction limited imaging mode is always applicable independently of the focal length used. Therefore, by using $\phi_{\text{PCF}} = 6.6$ cm, $d_{\text{CL-TA}} \approx d_{\text{AS-TA}} = 37.5$ m, and the lens with the focal length of 10 cm, we obtain $\phi_{ima} = .18$ mm for the diameter of the image of the partial contour field which is smaller than the shorter dimension of the HgCdTe detector used (.2 mm X .2 mm).

To minimize all signals that do not come from the lens, a restricting element has been installed in the cooled dewar of the detector to limit the field of view of the detector to the collecting lens. The final field of view of the detector has been adjusted to $\theta_d = 2 \arctan \frac{\phi_{\text{CL}}}{2f} \simeq 30°$.

Table IV

Description of the Photodetector Parameters.

Manufacturer	New England Research Center inc.
Model Number	MPV-0.2-B30
Detector Type	Photovoltaic HgCdTe
Element Size	.2 mm × .2 mm
Detector Resistance	1.1 KΩ
Frequency Bandwidth	DC to >100 MHz
Peak Wavelength	10.6 μm
Detector Temperature	77°K
Filter Spectral Bandwidth	.35 μm
Filter Wavelength Center	10.6 μm
Overall Responsivity	4.5 A/W
Noise Equivalent Power	6.7×10^{-13} W/$\sqrt{Hz}$

2.3 Detection and Noise Analysis Considerations

Previously, the mechanical and optical arrangement of this experimental set-up were analysed. In this section, the detection process will be investigated. A detailed description of the components of detection will be given and the expected level of noise will be evaluated. To do so, shot noise, detector noise and speckle noise will be discussed. The theoretical development found in this section is based principally on [2].

The detection system configuration follows the schematic description presented in Figure 2.4. The detector, a photovoltaic HgCdTe diode described in Table IV, converts the light signal into an electric signal. A spectral filter centered at 10.6 μm with .35 μm spectral width was placed in the liquid nitrogen chamber in front of the detector. Additionally, a field of view restricting element is introduced in a position adjacent to the spectral filter to lower the field of view to 30°. The overall responsivity of the detector with its components was evaluated experimentally (see Table IV). A transimpedance preamplifier applied a first electronic amplification to the detected signal before it was sent to the lock-in amplifier. This preamplifier fixes the electronic signal-to-noise ratio in a fashion that makes it negligible compared to the noise originating at the detector. The lock-in amplifier achieves the final desired amplification stage to accommodate the electric signal to the analogue to digital conversion process. The overall time response of the detector plus electronic amplification stage (preamp+lock-in) is essentially fixed by the lock-in time constant feature setting. The output of the lock-in amplifier gives 10 volts for a full scale reading. Finally, an A/D converter digitized the lock-in amplifier output and this digitized data is stored on hard disk. A power meter samples the laser output power

Table V

Description of Amplification and Digitalisation Parameters

Preamplifier	
Manufacturer	Perry Amplifier
Transimpedance Gain	200K V/A
Frequency Bandwidth	DC to 1MHz
Noise Performance (density)	1 nV/$\sqrt{\text{Hz}}$
Lock-In Amplifier	
Manufacturer	EG&G
Model Number	5210
Input Voltage Range	<10 nV to 3 V
Output Voltage	10 V (full scale)
Noise Performance	5 nV/$\sqrt{\text{Hz}}$
Time Constant	1 ms to 300 s
Equivalent Noise Bandwidth	250Hz(1ms),83Hz(3ms)
Analogue/Digital Converter	
Manufacturer	Data Translation
Model Number	DT2821-G-16SE
Number of Bits	12 (4096)
Conversion Equivalence	$10V \rightarrow 4096$
A/D Conversion Time	2.5 μsec

to keep track of time power fluctuations. Table V summarizes the characteristics of these electronic components.

If the electronic amplification is well designed, the noise limiting factors are essentially fixed by the detector characteristics. This noise originating from the detector can be classified in to three non-negligible types: the signal shot noise current (SSNC), the background shot noise current (BSNC), and the detector electronic noise current (DENC). Both SSNC and BSNC are the products of random statistical photon incidences at the detector. Only the origin of these photons (signal or background photon) will fix their noise classification. DENC is caused by electronic charge movement fluctuations in the detector material and its value is fixed by the manufacturer. These three sources of noise can be grouped together with the signal current (SCU) to form the current signal-to-noise ratio $(S/N)_c$.

$$\left(\frac{S}{N}\right)_c = \frac{(SCU)}{[(SSNC)^2 + (BSNC)^2 + (DENC)^2]^{1/2}} \qquad (2.12)$$

The signal current (SCU) is the current generated by the incoming desired light signal on the detector. Each of those four parameters (SCU, SSNC, BSNC, DENC) will be described and defined in the following subsections.

2.3.1 Signal Current (SCU)

The signal current is the current generated at the detector by the detected signal. In a mine imaging set-up such as the one shown here, the signal sought is the mine reflectivity contrast compared to the background. Using this definition and a well known relation establish in radar technology for signal level evaluation, the signal current is expressed as

$$\mathrm{SCU} = \overbrace{\mathrm{P_L} t_{\mathrm{L-TA}} t_{\mathrm{A}}^2 t_{\mathrm{TA-D}}}^{1} \quad \overbrace{\Delta\rho}^{2} \quad \overbrace{\frac{\mathrm{A_{AS}}}{d_{\mathrm{AS-TA}}^2}\eta}^{3} \quad \overbrace{\Re}^{4} \tag{2.13}$$

This relation is deduced from the range equation developed by Hudson [2]. For a first general description, this relation can be separated in four components. The first represents the illumination power of the target area, it takes into account the initial laser power ($\mathrm{P_L}$) and the losses resulting from the transmission through the optics used in the set-up ($t_{\mathrm{L-TA}}$ and $t_{\mathrm{TA-D}}$) and from the transmission of the atmosphere (τ_{A}). The second is the target reflectivity contrast to the incident illumination; it depends exclusively on the characteristic of the surfaces illuminated. The third represents the radiometric parameters of the set-up; it is composed of the reflected radiation collected ($\frac{\mathrm{A_{AS}}}{d_{\mathrm{AS-TA}}^2}$) and the geometry mismatch factor (η) between the illumination spot (ϕ_{1/e^2}) and the contour field (CF) . Finally, the fourth is caused by the transformation of the optical signal to an electric signal; this parameter depends on the detector characteristics only.

In direct relation to this experimental set-up, the transmission of the optical set-up from the laser to the target area ($t_{\mathrm{L-TA}}$) has been evaluated by measuring the average power of the laser beam at the foot of the tower (400 mW) and dividing it by the initial average power of the laser (3 W). $t_{\mathrm{L-TA}} = 13\%$ is obtained. In a similar fashion, we evaluated the transmission of the optics from the target area to the detector ($t_{\mathrm{TA-D}}$) to be 24%. To take in account the signal loss due to the mismatch between the contour field ($\phi_{\mathrm{CF}} = 1.9$ cm) and the laser spot size at target area ($\phi_{1/e^2}^{min} = 2.23$ cm), η (the field of view matching factor) is fixed, using relation A.4, to 85 %. The contrast in reflectivity ($\Delta\rho$) is the parameter which characterize this experiment. It is the unknown parameter upon which feasibility of mine detection using active infrared imaging principally depends. $\Delta\rho$ is defined as the mine reflectivity (ρ_{mine}) minus the background reflectivity ($\rho_{background}$). $\Delta\rho$ is then strongly dependent on the type of background and the type of mine. Moreover, this reflectivity contrast will be strongly dependent on the angle of view with which we illuminate and look at the minefield. In the analysis chapter, it will be shown that the experimental results from this set-up will be calibrated as a function of this parameter; this is to allow extrapolation of the feasibility of mine detection with this technique to other active imaging configurations. Each of the parameters in relation 2.13 are defined and evaluated in the list of symbols.

Table VI

Manufacturer's Properties of the Detection Electronics.

		Lock-In Time Constant		
		1 ms	3 ms	10 ms
Δf	(6 db)	250 Hz	83 Hz	24 Hz
	(12 db)	125 Hz	42 Hz	10 Hz
$\tau_{1/2}$	(6 db)	1 ms	2.5 ms	10.5 ms
	(12 db)	1.75 ms	5.2 ms	17 ms

2.3.2 Current Shot Noise (SSNC and BSNC)

As mentioned previously, the current shot noise ($< i_s >$) is a well known phenomena. It has been described in detail and experimentally verified. In a general fashion, the shot noise is defined as follows

$$< i_s >= (2e\mathrm{I}\Delta f)^{1/2} \tag{2.14}$$

where e is the charge of an electron, Δf is the frequency band of the measuring instrument and I is the total current carried by the conductive medium. This general definition is used to evaluate the signal shot noise current (SSNC) by simply replacing I in this relation by the current generated at the detector by the reflected laser signal. This is formulated as

$$< i >^2_{\mathrm{SSNC}}= 2e\Re\rho \mathrm{P_L} t_{\mathrm{L-TA}} t_{\mathrm{A}}^2 t_{\mathrm{TA-D}} \frac{\mathrm{A_{AS}}}{d^2_{\mathrm{AS-TA}}} \eta \Delta f \tag{2.15}$$

In this expression, the total reflectivity (ρ) of the illuminating area is used because I, in this definition, is the total current generated at the detector by the reflected laser signal and not only by the signal of interest as in equation 2.13.

The shot noise created by the background comes principally from the thermal radiation of the target area seen by the detector[4]. This signal can be evaluated by quantifying the thermal radiant exitance (the radiative power per area and per wavelength emitted by a body) of the target area and integrating this exitance over the surface seen by the detector [5]. To do so, we will assume a blackbody characteristic to the target area. The spectral radiant exitance of a blackbody is described as

[4]The irradiation originating from solar reflection is greatly reduced by the spectral filter to a value negligible compared to the thermal irradiation (see appendix C)

[5]Terms and definitions used in this subsection can be found in Chapter 1 of [3].

$$M_{\lambda}^{B}(\lambda, T) = \frac{2\pi hc^2}{\lambda^5(\, e^{\frac{h\nu}{kT}} - 1)} \quad \left(\frac{W}{m^3}\right) \tag{2.16}$$

Using the parameters shown in the list of symbols, M_{λ}^{B} is evaluated at 3×10^7 W/m^3. With the .35 μm spectral width filter placed in front of the detector, the radiant exitance of the target area at 10.6 μm is $M_{10.6,.35}^{B} = 11$ W/m^2. So, the total background current (BC) generated at the detector will be defined in a fashion comparable to the signal current (equation 2.13) as

$$BC = \overbrace{\Re}^{1}\ \overbrace{\xi}^{2}\ \overbrace{M_{10.6,.35}^{B} t_A t_{TA-D}}^{3}\ \overbrace{\frac{A_{AS}}{d_{AS-TA}^2} A_T}^{4} \tag{2.17}$$

In this relation ξ, the emissivity of the background, is fixed at $1/\pi$ because of the blackbody characteristic assumption. A_T in this relation is the area seen by the detector (virtual or real) in its conjugate plane through the collecting lens. Here, virtual or real area are mentioned because even if the image of the detector at target area is larger than the partial contour field (PCF), the detector will still receive the same amount of radiation contained in the solid angle sustained by this image of the detector at the target plane (even if the real radiation originates from a screening optical component at the field stop). With the values given in the list of symbols for the parameters of equation 2.17, BC is evaluated to 20 nA. Because this background signal is not modulated, the lock-in amplification process will reduce this signal to a final value close to zero; however this is not the case for the shot noise associated with the current created at the detector by this thermal background radiation. With the definition introduced in relation 2.14, the background shot noise current is fixed by the following relation:

$$< i >_{BSNC}^{2} = 2e\Re\xi M_{10.6,.35}^{B} t_A t_{TA-D} \frac{A_{AS}}{d_{AS-TA}^2} A_T \Delta f \tag{2.18}$$

2.3.3 Detector Electronic Noise Current (DENC)

Finally, the last source of noise at the detector is the one created internally by its electronics. Its level depends essentially of the wavelength to be detected, the size of the detector and the fabrication techniques associated with the detector itself. Thus, the intensity of this noise is fixed by the manufacturer. The evaluation of the electronic noise current created by the detector is characterized by the relation below

$$< i >_{DENC} = (NEP)\Re\sqrt{\Delta f} \tag{2.19}$$

where NEP is the noise equivalent power per $\sqrt{\text{Hz}}$ as given by the manufacturer (see Table IV).

By grouping relations 2.15 2.18 and 2.19 to the definition of $(S/N)_c$ in equation 2.12, the following equation for the complete current Signal-to-Noise ratio $(S/N)_c$ is obtained

$$\frac{\Re\,\Delta\rho\,P_L\,t_{L-TA}\,t_A^2\,t_{TA-D}\,\frac{A_{AS}}{d^2_{AS-TA}}\,\eta}{\left[2e\Re\rho P_L\,t_{L-TA}\,t_A^2\,t_{TA-D}\,\frac{A_{AS}}{d^2_{AS-TA}}\,\eta\,\Delta f + 2e\Re\xi M^B_{10.6,.35}\,t_A\,t_{TA-D}\,\frac{A_{AS}}{d^2_{TA-D}}\,A_T\,\Delta f + (NEP)^2\Re^2\,\Delta f\right]^{1/2}} \tag{2.20}$$

This last relation shows the general model describing the electric current signal-to-noise ratio. An important piece of information given by this relation is the expected detection efficiency. A good evaluation of this property for the imaging set-up can be obtained by evaluating the level of noise in the configuration called "low signal situation" $((\rho P_L) \rightarrow 0)$. In this case, SSNC becomes negligible compared to the two other sources of noise and can be ignored. By replacing the values found in the list of symbols in the expression for these noise sources, the following equation is obtained

$$\frac{< i >_{BSNC}}{\sqrt{\text{Hz}}} = 0.08\ \text{pA}/\sqrt{\text{Hz}} \tag{2.21}$$

$$\frac{< i >_{DENC}}{\sqrt{\text{Hz}}} = 3\ \text{pA}/\sqrt{\text{Hz}} \tag{2.22}$$

Consequently, this active IR imaging system is not background noise limited, but is limited by the noise of the detector itself. This is not unexpected with the configuration used in this optical set-up because of the narrow field of view and narrow spectral window seen by the detector, as well as the low level of detection available at the wavelength 10.6 μm.

From the result previously stated and using the specifications of the amplification stage in Table V, the minimum noise level at the output of the preamplifier for small signals is evaluated to

$$\frac{< V >_{preamp}}{\sqrt{\text{Hz}}} = 200\ \text{KV}\ \frac{< i >_{DENC}}{\sqrt{\text{Hz}}} = 0.6\ \mu\text{V}/\sqrt{\text{Hz}} \tag{2.23}$$

2.3.4 Speckle Noise

The speckle effect is a well known phenomena. Many articles have been published to characterize its origin, mechanism and methods to reduce it [4, 5, 6, 7, 8, 9]. In this

section, only a qualitative approach is used to describe the physics associated with this phenomena, the consequences associates with this effect is discussed. The speckle appears when we illuminate a rough (compared to the light wavelength used) surface with coherent light. In this case, points of this rough surface will act as a coherent source creating an interfering pattern of reflection. Due to the different path lengths travelled by the light originating from these point sources randomly distributed on the rough surface, the reflected light will form an interference pattern (the speckle pattern) composed of randomly distributed intensity minima and maxima. Consequently the signal at the detector, for this experiment, can show strong fluctuations depending on this random distribution of intensity minima and maxima incident on the collecting lens. This uncertainty in collected intensity reflected is responsible for what is called speckle noise. To reduce the noise associated with speckle, two implied processes are performed during the signal acquisition in this experiment. These two processes are spatial and temporal integration and they are discussed below for the present experiment.

To evaluate the importance of the speckle noise present in our active imaging system, the first characteristic to evaluate is the average dimension of a speckle cell (maximum intensity area) at the collecting lens. This can be done roughly by evaluating the maximum spatial frequency which the light reflected from the illuminating spot can create at the plane of the collecting lens. This is evaluated simply from Fourier optic theory as

$$\Delta x = \frac{\lambda d}{\phi} \tag{2.24}$$

where

λ	wavelength
d	distance between observation screen and illuminated area.
ϕ	illuminated spot size
Δx	average diameter of a speckle

With the parameters involved in our imaging system ($\lambda = 10.6\,\mu$m, d = 37.5 m, $\phi_{1/e^2}^{min} = 2.23$ cm), an average diameter of 1.8 cm is obtained for the high intensity speckle spot. An other important characteristic of speckle noise is that this type of noise is proportional to the signal. Because of this property, we usually evaluate the signal-to-noise ratio resulting from speckle (S/N_{spe}) rather than the speckle noise itself.

As mentioned previously, there are two speckle noise reduction processes performed in this experiment. The first process is a spatial integration performed by the collecting lens. The fact that the lens integrates an intensity distribution of the speckle pattern over its aperture contributes to reducing the variance in the value of the reflectivity of the area illuminated at the target area. As demonstrated in [5], the

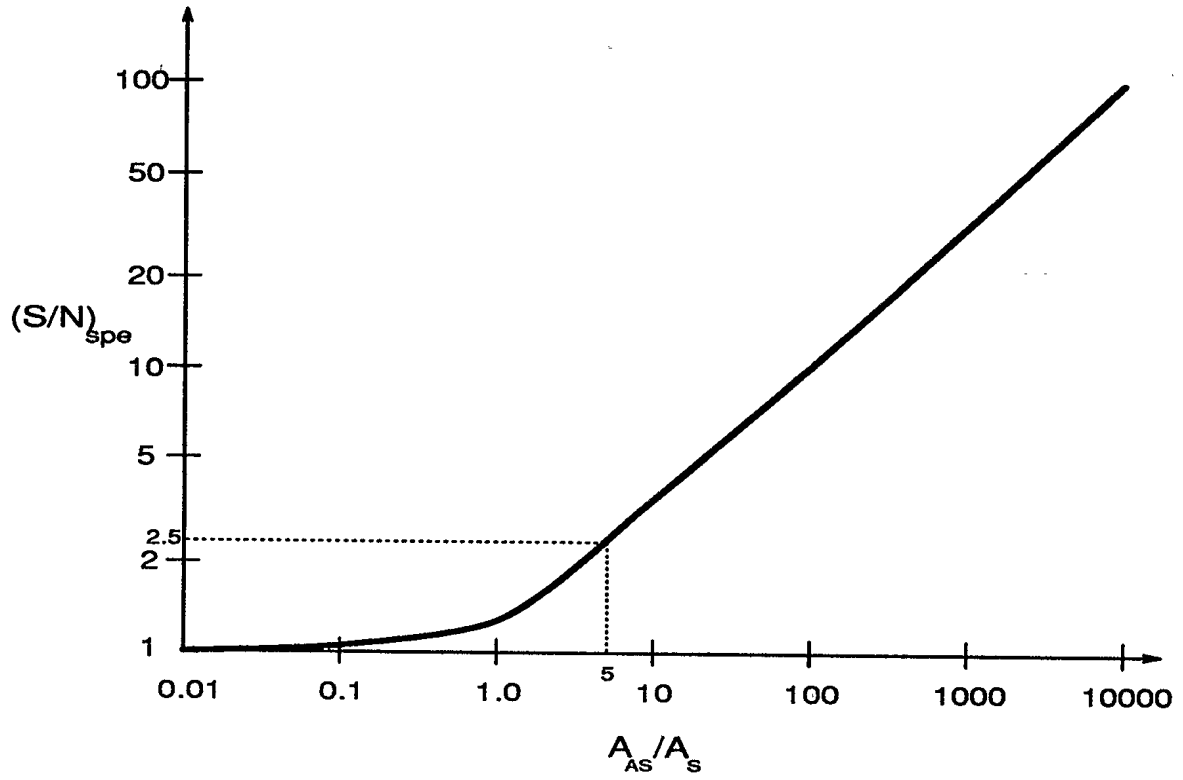

Figure 2.9

$(S/N)_{spe}$ Ratio vs the Ratio AS Area/Average Speckle Area.

speckle signal-to-noise ratio of the signal detected can be evaluated approximately using Figure 2.9. In this graph, A_{AS} is the effective area of the collecting lens and A_S can be approximated as the corresponding area of a circle having a diameter equal to Δx, the average diameter of a speckle. Using the numerical values for these two parameters ($A_{AS} = 12.6$ cm^2, $A_S = 2.5$ cm^2), an evaluation of the speckle signal-to-noise ratio after spatial averaging noise reduction is obtained:

$$\left(\frac{S}{N}\right)_{spa} \simeq 2.5 \tag{2.25}$$

The level of noise coming from the speckle after a spatial integration is clearly quite high. Fortunately, a second process of speckle noise reduction is performed during image acquisition. This second process is called temporal integration. Temporal integration is performed because of the displacement of the illuminating spot at the target area during the detection integration time ($\tau_{1/2}$). This procedure allows a second average of the speckle signal after spatial integration and improve even more the signal-to-noise ratio. The exact description of the noise reduction performed as a function of the displacement has not been developed so far for the particular configuration used in this experimental set-up, but it can be assumed that this noise

reduction increases with the displacement of the laser spot during integration and decreases with the expansion of the laser spot. This dependence will be fully investigated, and a model will be realized and verified to quantitatively describe this second speckle noise reduction technique.

3. Presentation of Active IR Images

This chapter will show the best active IR images of the mines reported in section 2.1 obtained by the experimental set-up described previously. Only qualitative remarks on detection and identification of these mines will be reported. In the next chapter, a more quantitative analysis of these experimental results will be performed to allow extrapolation of the detection and identification capabilities with other set-up configurations.

Active IR images shown in this chapter were submitted to only a minor amount of image processing. Specifically, only sample averaging and contrast adjustments have been performed. In this averaging, samples distributed across a 2 cm scanned distance at the target area were added and an interpolation between the averaged values is performed to bring back the linear density of samples to 1 sample per cm of scanned distance [1]. When analysis is performed on the images shown in this chapter, the reader should keep in mind that the electronic digitized images contain a much better visible contrast than the printed images; however, conclusive remarks can still be seen from visual inspection of the printed images.

For most of each active IR image shown in this chapter, a corresponding visible wavelength photograph is shown. These photographs are very useful for object identification on the IR image. For each IR image, five aluminium disks are used to delimit the scanned area. These aluminium disks show a highly diffuse reflectivity which make their identification obvious. The zone of the target area occupied by the aluminium disk at the center bottom of these images represents the vertical position of the last mirror (M7 in Figure 2.2). Thus, objects parallel to the ground in this area will show a perpendicular point of view to the laser beam. Consequently, highly specular objects will demonstrate high reflected signals around this position.

For each image the lock-in sensitivity, the detection response time ($\tau_{1/2}$), and the number of samples per scanned distance is given. As mentioned in section 2.2.1, for all images shown in this chapter, the scanning speed (SS) is adjusted to the integration

[1] A 2 cm scanned distance corresponds approximately to the optimum resolution of the imaging system.

time constant ($\tau_{1/2}$) to keep the product $2 \times \tau_{1/2} \times$ SS equal to 4 cm. IR images of the different types of mine can be found on the following figures: TMN-46 (Figures 3.1 and 3.6), PM-60 (Figures 3.2, 3.3, and 3.6), TMB-D (Figures 3.2, 3.3, and 3.6), PMN-6 (Figures 3.4, 3.5, and 3.6), OZM-3 (Figures 3.4, 3.5, and 3.6), PFM-1 (Figures 3.4, 3.5, and 3.6) [2]. Soil and prairie grass have been used as backgrounds. All the mines used to make the IR images shown here were laid directly on the ground without special adjustment. Their observed surface is thus close to parallel to the ground with a small angular distribution caused by the soil roughness. However, this angular distribution is larger for the mines laid on grass. A detailed description of each of these active IR images is introduced following the group of figures.

[2] A close view of each of those mines is shown in appendix D

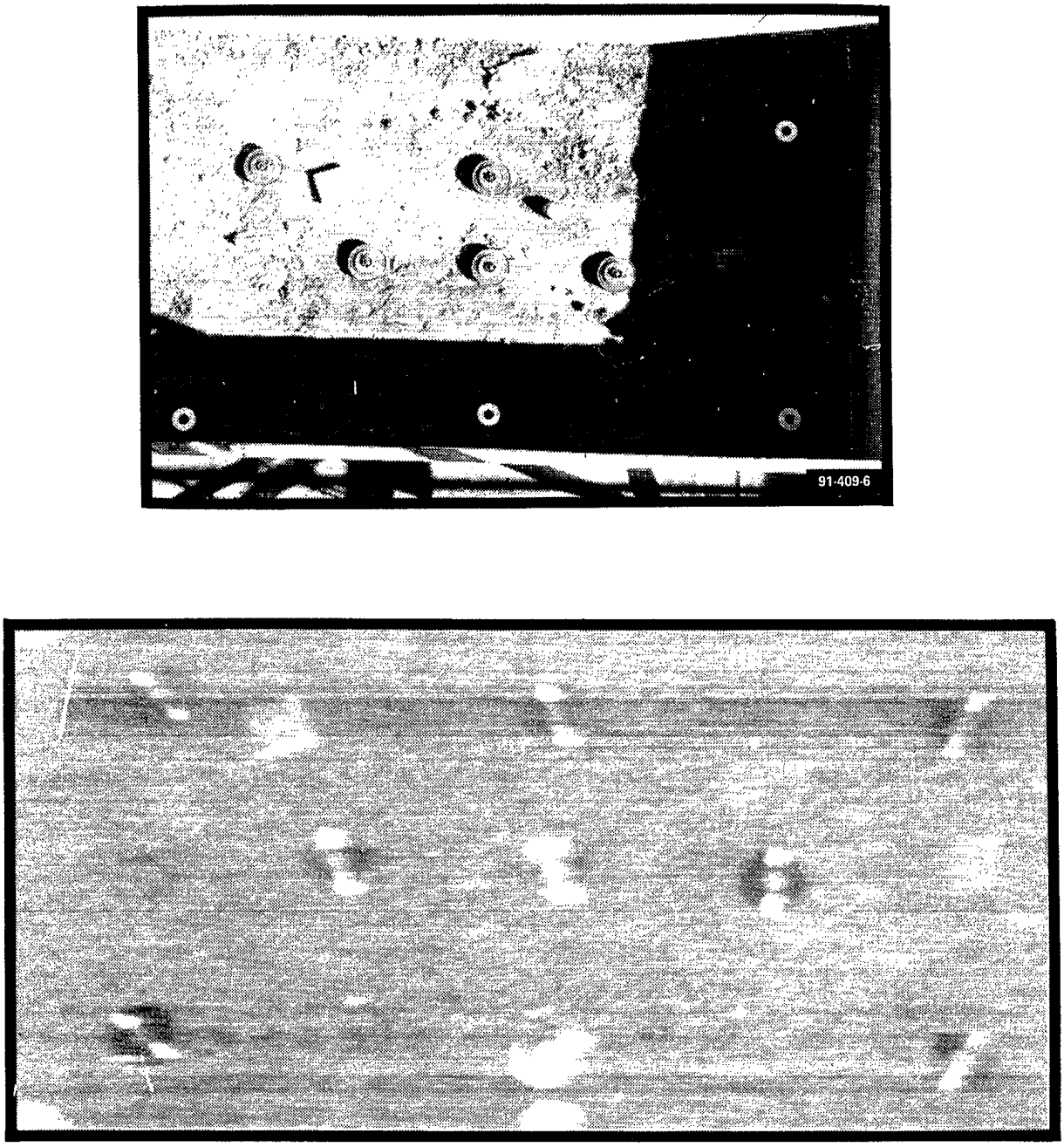

Figure 3.1

Active IR image of TMN-46 mines on a soil background (lower image). The upper image presents the same area in visible light.

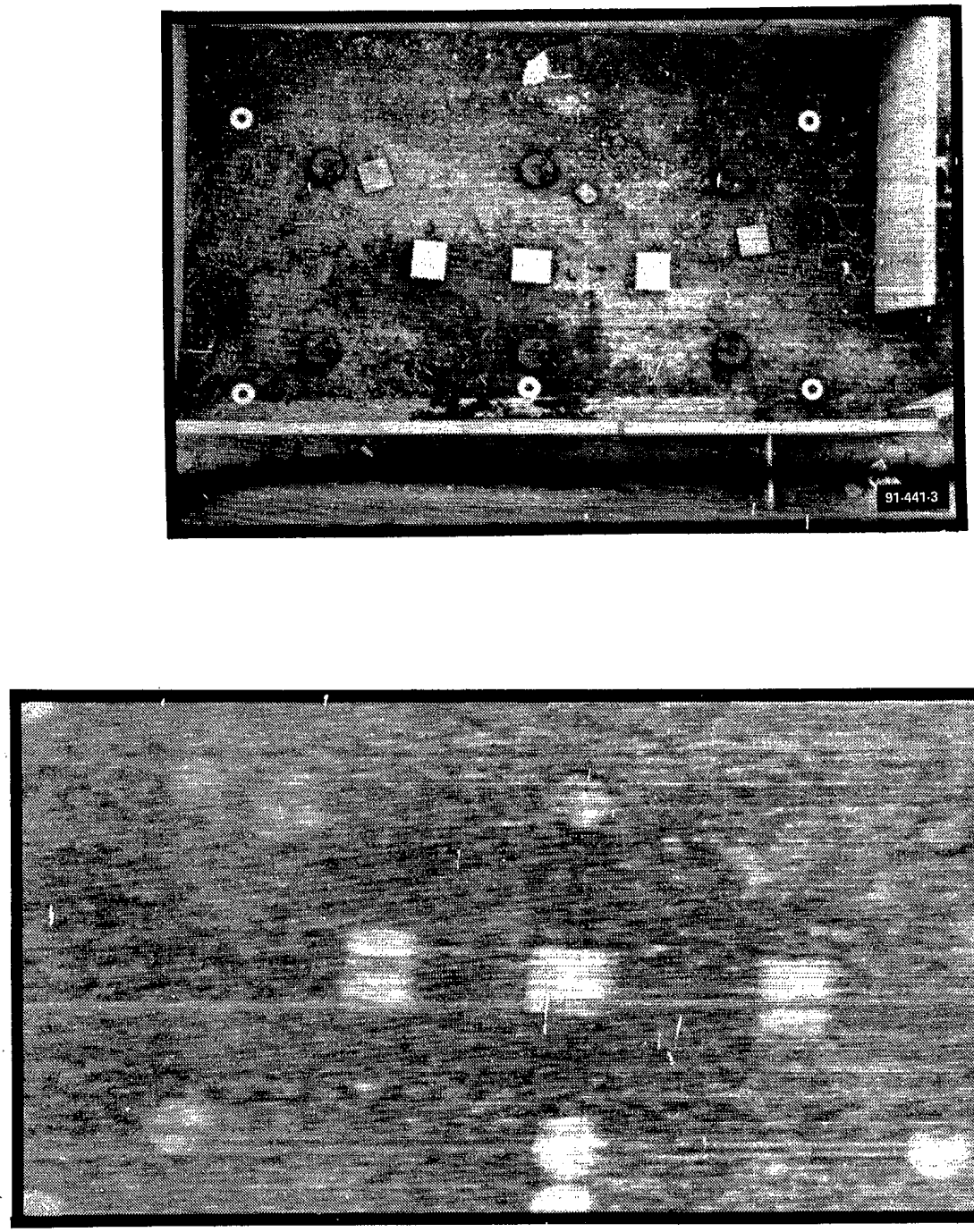

Figure 3.2

Active IR image of PM-60 and TMB-D mines on a soil background (lower image). The upper image presents the same area in visible light.

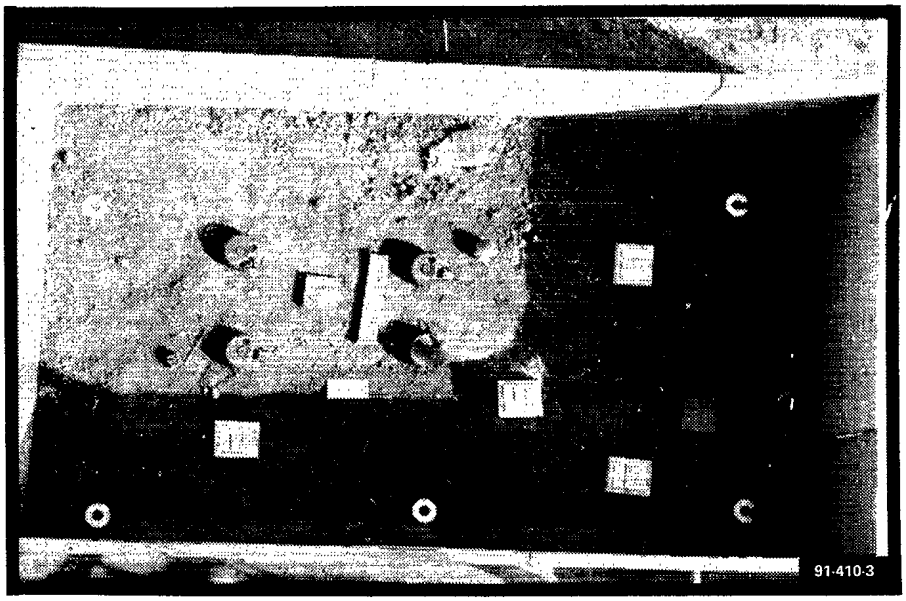

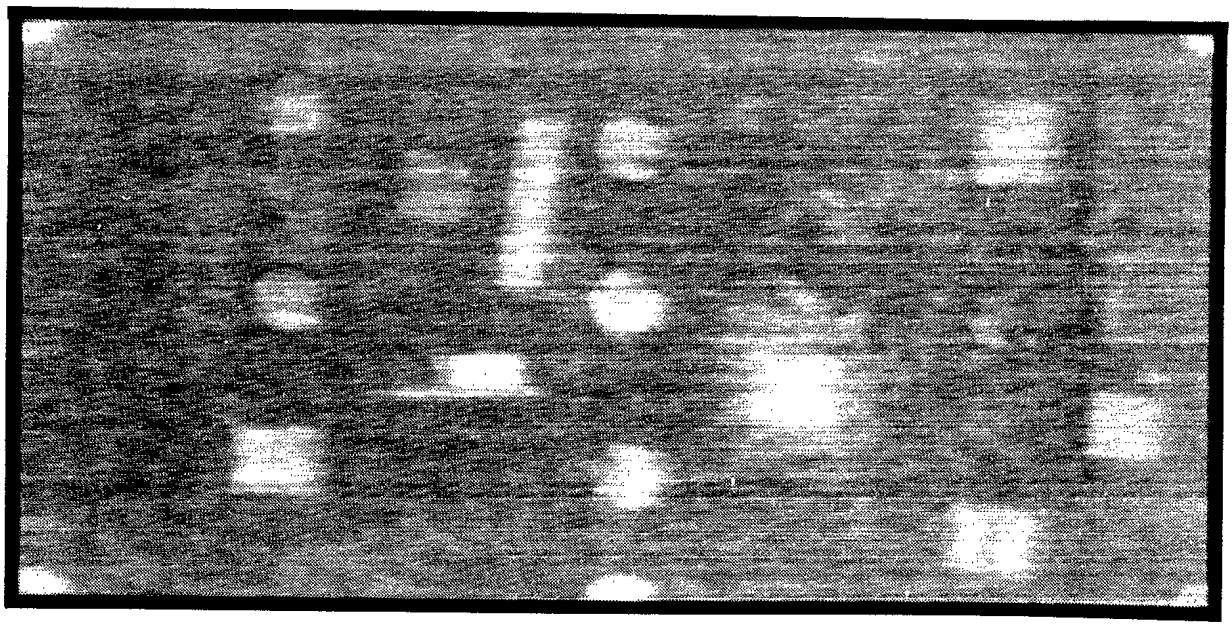

Figure 3.3

Active IR image of PM-60 and TMB-D mines on a soil and prairie grass background (lower image). The upper image presents the same area in visible light.

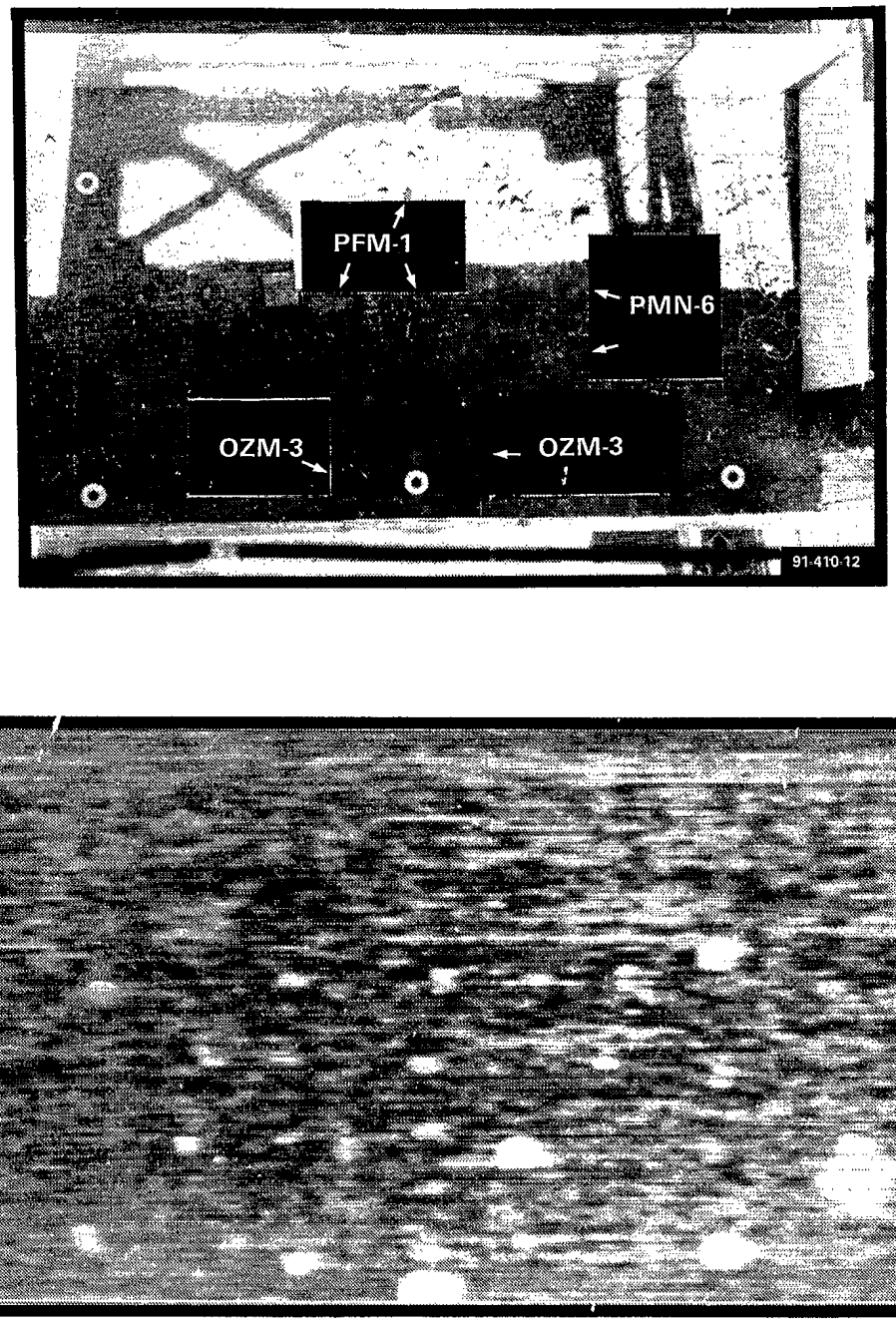

Figure 3.4

Active IR image of PMN-6, PFM-1 and OZM-3 mines on a soil background (lower image). The upper image presents the same area in visible light.

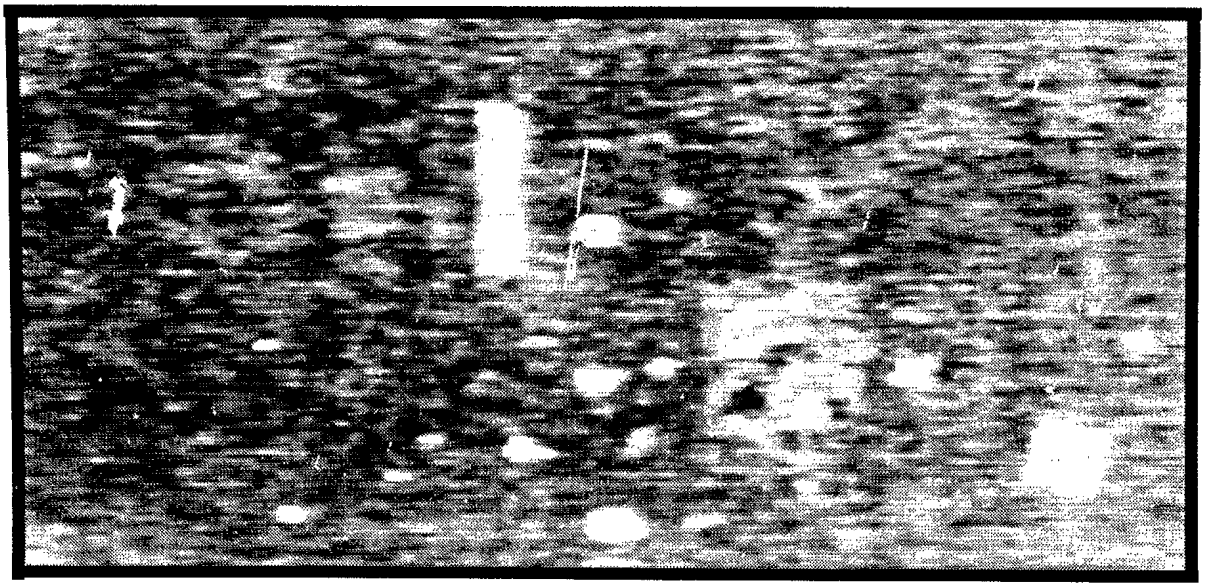

Figure 3.5

Active IR image of PMN-6, PFM-1 and OZM-3 mines on a soil and prairie grass background (lower image). The upper image presents the same area in visible light.

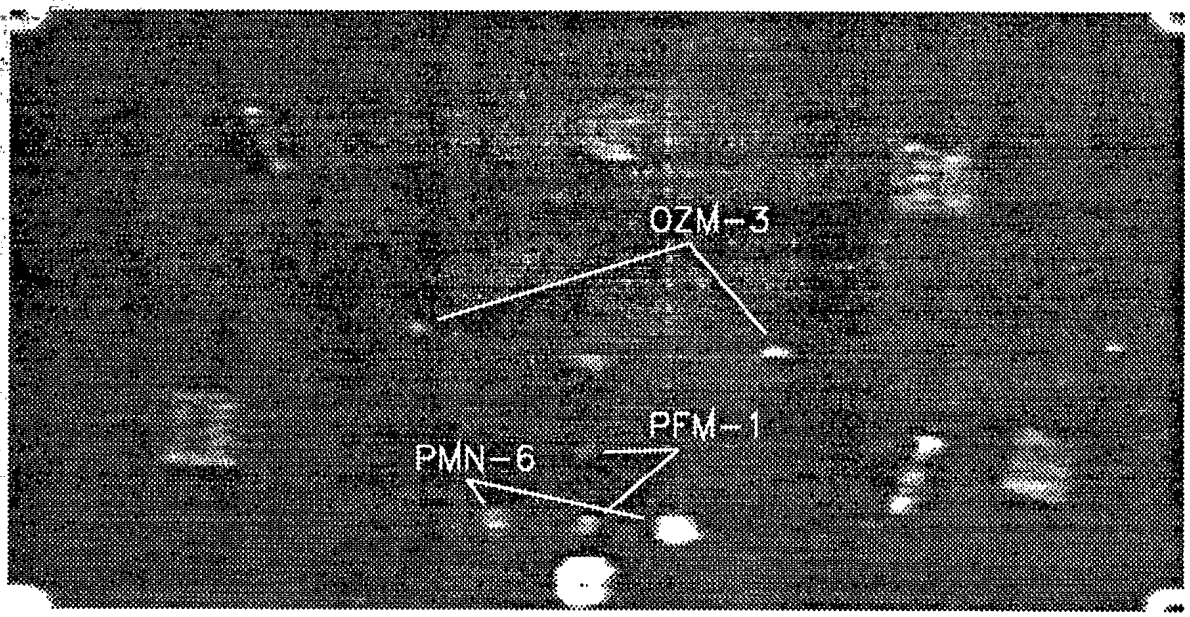

Figure 3.6

Active IR image of TMN-46(2), PM-60(2), TMB-D(2), PMN-6(2), PFM-1(2) and OZM-3(2) mines on a soil background. No photograph in the visible spectrum is available for this IR image.

Description of the active IR images:

Figure 3.1

Type of Mine:	TMN-46
Background:	Soil
Lock-In Sensitivity:	30 mV
Detection Response Time:	1 ms
# Samples per 2 cm Displacement:	3

This active IR image shows a type of mine easily detectable and identifiable (TMN-46) on a soil background. This is the result of its large dimension and highly specular surface. The high specularity is responsible for the dark appearance of the mine. This mine presents a good example of negative contrast. When the laser beam hits its surface, most of the light signal is redirected away from the detection axis as a mirror would do. The only time a portion of the signal will be detected is when the laser beam hits a surface perpendicular to its direction of propagation. That explains the two highlighted regions on its image. An other observation is that the wooden boards are easily detectable, but rocks show in this image have a weaker contrast and cannot be observed. An other important remark to mention on this IR image is that mines in shadow

are as easy to see as the ones directly under the sun. This confirms the active imaging technique used and the previously mentioned negligible effect of the sun illumination compared to the laser illumination.

Figure 3.2

Type of Mine:	PM-60 and TMB-D
Background:	Soil
Lock-In Sensitivity:	30 mV
Detection Response Time:	10 ms
# Samples per 2 cm Displacement:	6

The TMB-D, as the TMN-46, is easily detectable and identifiable on this image. But, contrary to the TMN-46, the detection of the TMB-D results from its diffuse reflectivity. The wood surface of this type of mine will reflect a large part of the laser light in a wide cone which can be detected even when illuminated at a large angle from the perpendicular to its surface. On this image, even the board orientation of this particular mine can be observed. The highlighted horizontal lines were caused by a saturation of the detection system due to a direct backward reflection of the laser beam by the hinge present on the TMB-D. The PM-60 presents more difficulty to detect and identify than the TMN-46 and TMB-D. This result can be explained by the characteristic of the surface of the PM-60. It surface is mostly specular but with a diffuse reflectivity comparable to the background. Its reflectivity contrast to the background is thus difficult to observe for a field of view greater than 0^o to its surface. However, it is still possible to detect and identify this type of mine in this image; moreover, for some of the PM-60, the position of the handle can be identified by inspection of the electronic image.

Figure 3.3

Type of Mine:	PM-60 and TMB-D
Background:	Soil and Prairie Grass
Lock-In Sensitivity:	20 mV
Detection Response Time:	3 ms
# Samples per 2 cm Displacement:	6

This image shows a second representation of PM-60 and TMB-D mines with active IR techniques. Prairie grass samples have been placed in the scanned area to observe the reflectivity of this different background compared to the mines. The grass presents a slightly higher diffuse reflectivity than soil but not enough to hide the type of mine used in this image. Some alien objects had been placed in the target area to compare their reflectivity to mines. A brick does not show but a wood board is still easily visible. A metal bar can appear depending of its orientation because of its highly specular reflectivity. This shows the need

for high spatial resolution if minefields are to be reliably detected. Again, each of these types of mine can be detected and identified on this image.

Figure 3.4

Type of Mine:	PMN-6, OZM-3 and PFM-1
Background:	Soil
Lock-In Sensitivity:	30 mV
Detection Response Time:	1 ms
# Samples per 2 cm Displacement:	6

Active IR images of anti-personnel mines are shown in this figure. These types of mines are difficult to detect and even more difficult to identify because of their small dimensions and their reflectivity characteristics. This printed representation carries less information than the computer file but it is still possible to establish some facts. The PMN-6 can be detected but it is highly sensitive to the angle of view. Its high reflectivity and high specular property make this mine easy to detect and identify for angles of view close to 0° from the perpendicular to its upper surface. The OZM-3 mines are easily detectable in a standing up position but their identification can be difficult because of their small spatial dimension. The PFM-1 shows a lower reflectivity than the two other types of mine but can still be detected. However, its size gives identification problems for the resolution used in this imaging set-up.

Figure 3.5

Type of Mine:	PMN-6, OZM-3 and PFM-1
Background:	Soil and Prairie Grass
Lock-In Sensitivity:	50 mV
Detection Response Time:	3 ms
# Samples per 2 cm Displacement:	6

This figure shows a second active IR image of anti-personnel mines. Again, this printed image shows less information than the computer file. Many PMN-6 and PFM-1 are detected and could be identified depending on the angle of view. It is more difficult to detect PMN-6 and PFM-1 types of mines on grass. This is probably related to the higher reflectivity of the grass and its uneven surface which will generate large angle of view for these light laid mines, and consequently reduce considerably their reflectivity. The OZM-3 placed on the side (the OZM-3 located on grass) would deflect the laser beam away, depending on its orientation. The location of the mine appears then as a dark area in the shape of the mine (negative contrast).

Figure 3.6

Type of Mine:	TMN-46(2), PM-60(2), TMB-D(2), PMN-6(2), OZM-3(2) and PFM-1(2)
Background:	Soil
Lock-In Sensitivity:	10 mV
Detection Response Time:	3 ms
# Samples per 2 cm Displacement:	6

In this active IR image, all the previous types of mines are presented. Unfortunately, no visible light photograph is available. TMN-46, PM-60 and TMB-D are easily detectable and identifiable. The two OZM-6 are also easy to detect (in standing position) even if they are placed at large angle of view. The PMN-6 and PFM-1 are also easy to detect and identify. This is basically created by their position close to the vertical area from the last mirror (mirror M7 in Figure 2.2). The shape of the PFM-1 close to the center aluminium disk can almost but not quite be visualized in the electronic image version.

We have seen, with these active IR images, that each type of mine present can be detected and identified within the conditions involved in this experimental set-up. Anti-tank mines as TMN-46, TMB-D and PM-60 are the easiest to detect and identify. They can be observed for all possible angles of view present in this imaging set-up (up to 10°, see Figure 2.3). For anti-personnel mine types such as PMN-6 and PFM-1, detection depends strongly on the angle of view. The closer this angle is from the perpendicular to their principal surface, the higher will be the signal detected. Their identification could be difficult but adequate image processing should solve this problem. Grass presents a little more reflectivity than soil but not enough to hide most of the mines shown here. However, its irregular surface can impose large angles of view for anti-personnel mines and lower the detection efficiency. The OZM-3 type of mine shows high reflectivity in a standing position and low reflectivity on its side for most angles of view tested in this experiment. These properties give good detection for this type of mine but its small viewing dimension in standing position could make its identification difficult. From the direct analysis of the IR images shown, a lower false alarm level can only be achieved by a good discrimination between mines and unimportant foreign objects. This good discrimination can only be achieved by good spatial resolution (few centimeters).

In the next chapter, a more quantitative interpretation of the experimental conditions involved in this experiment is given. That will allow an extrapolation of the required configuration for other experimental set-ups.

4. Analysis of Experimental Results

In the previous chapter, the most representative active infrared images obtained with the experimental set-up described in this report were presented. However the results introduced were qualitative and only presented to establish approximately the mine detection and identification capabilities of the particular imaging set-up described. In this chapter, to make those results useful in a more general fashion, we will characterize and identify the important parameters of this optical set-up which will allow the prediction of the mine detection and identification capabilities expected with other active IR imaging systems presenting different optical configurations. To do so, quantitative evaluations of the noise level, background signal and resolution observed in those active infrared images obtained experimentally will be performed and compared to those predicted by the theory developed in Chapter 2. After establishing the validity of this model, the important parameters to monitor when a new imaging system with other optical configuration is proposed will be identified.

4.1 Experimental Characterization of the Imaging Set-Up

Before transferring the results obtained in this experimental set-up to other imaging system using the theory proposed in Chapter 2 , we will evaluate the accuracy of the model. For this purpose, noise, background signal and resolution obtained experimentally will be evaluated and compared to the values predicted by the theoretical model.

4.1.1 Experimental Noise Evaluation of the Imaging Set-Up

From the four kinds of noise identified in section 2.3 (SSNC, BSNC, DENC, and speckle noise), only those present in the low signal situation (see definition given at page 23) will be evaluated experimentally. This evaluation is important because this type of noise is mainly responsible for the limitation in detection capabilities of an imaging system.

Table VII

Experimental backscattering and low signal noise observed when the CO_2 laser is reflected away from its incoming direction.

Experimental Backscattering Signal	500 μV or 2.5 nA	($\tau_{1/2} = 1$ ms)
Experimental Low Signal Noise	60 μV or 19 pA/$\sqrt{\text{Hz}}$	($\tau_{1/2} = 1$ ms)

At this level of signal, for our set-up, section 2.3 shows that the detector is the principal source of noise (DENC). To evaluate the level of this source of noise, mirrors were placed at the target area to deflect the laser beam away from its counter-direction. In this case, the reflected laser signal should be reduced ideally to zero. Thus theoretically, the average total signal detected should be zero with an average noise level caused principally by the detector. However, the experimental results do not agree with these predictions. A residual signal of the order of 500 μV, which corresponds to a current of 2.5 nA generated at the detector, is detected. After analysis we associate this residual signal to two potential causes:

- misalignment of optical set-up.
- mirrors backscattering along optical set-up.

These two causes imply a return of the modulated laser signal to the detector. Moreover, those two potential causes are probably shown in order of importance. In fact, the misalignment is very critical, since not much space is allowed between the laser beam and the mirror edges at the scanner location. A slight error in the laser alignment will produce sufficient light return from the scanner wall to easily create an artificial background signal. The mirror backscattering problem is probably caused by dust accumulation on their surface by the wind. The mirror surface can thus optically degrade, create scattered light at the laser incidence position and return this light to the detector as a background signal. These problems could be easily solved by simplifying the optical set-up. Reducing the optical trajectory by moving the optical shelter on top of the tower seems to be the ideal solution to solve these two problems.

The level of noise evaluated from the mirror image is about 60 μV for a detection bandwidth of 250 Hz ($\tau_{1/2} = 1$ ms). This amount of noise corresponds to a detector current noise of 19 pA/$\sqrt{\text{Hz}}$. It is easy to verify that this level of noise cannot come from shot noise associated to the background signal observed ($< i > /\sqrt{\text{Hz}} = (2eI)^{1/2} = .03\,\text{pA}/\sqrt{\text{Hz}}$). Moreover, this noise observed is over 6 times greater than the detector electric noise expected theoretically ($< i >_{\text{DENC}} /\sqrt{\text{Hz}} = 3\,\text{pA}/\sqrt{\text{Hz}}$). So far, two sources of noise has been identified to justify this excess noise.

- speckle noise associated to the backscattered signal observed and
- external electronic noise.

In our present analysis, those two sources could contribute in any proportion to this excess noise observed. The reason for this uncertainty is the difficulty in characterizing the speckle noise involved. Further experimental studies in laboratory should be done to characterize the suppression of speckle noise caused by the laser beam spot movement during detection time integration. On the other hand, the presence of high voltage modulation (for the electro-optic modulator) in the proximity of detection components can also be responsible for a large part of this excess noise. To reduce this potential contribution, improved electro-magnetic shielding will be designed.

4.1.2 Experimental Evaluation of the Imaging Resolution

In section 2.2.1, the expected imaging resolution is evaluated as a function of the laser spot size at target (ϕ_{1/e^2}), the scanning speed (SS) and the detection integration time ($\tau_{1/2}$). We established the laser spot size as the resolution limit of the image in the direction perpendicular to the scanning direction. In the direction parallel to the scanned lines, the imaging resolution is characterized as a sum of two terms (equation 2.2): the laser spot size and the integration time of the detection components times the scanning speed. To characterize experimentally the resolution of the imaging system, an image of a highly diffuse reflectivity grating formed with a flame sprayed aluminium plate covered with low reflectivity bands of decreasing lateral dimension is achieved. These bands were placed in such a way as to have a distance of 5.5 cm between the first and second high reflectivity area, 4.5 cm between the second and third, 3.75 cm between the third and fourth and 2.75 cm between the fourth and fifth. The width of these low reflectivity bands were 3 cm, 2.5 cm, 2 cm, 1.5 cm, and 1 cm.

Figure 4.1 shows the active image intensity profile of the aluminium plate, achieved with the optical system, with the low reflectivity bands placed perpendicular to the scanned direction. For this particular study, multiple images of the plate were made with different scanning speeds for a detection integration time constant of 1 ms. This process allowed the change of the product $2 \times \tau_{1/2} \times \mathrm{SS}$ (and the total resolution) and kept the noise associated with the electronic constant (Δf kept at 250 Hz). We can observe that the resolution increases with the reduction of the corresponding travelled distance during the detection integration time as expected. From the second intensity profile (that where $2 \times \mathrm{SS} \times \tau_{1/2} = 1.33$ cm) and with the equation 2.2 describing the total imaging resolution and the resolving criteria described in section 2.2.1, the laser spot size ($\phi_{1/e}$) can be evaluated to less than 2.5 cm. This assumption is compatible with the optical resolution in the direction perpendicular to the scanned area observed in Figure 4.2 [1]. This size for the laser spot at the target is slightly

[1]The resolution in the direction perpendicular to the scanned lines is more difficult to analyse

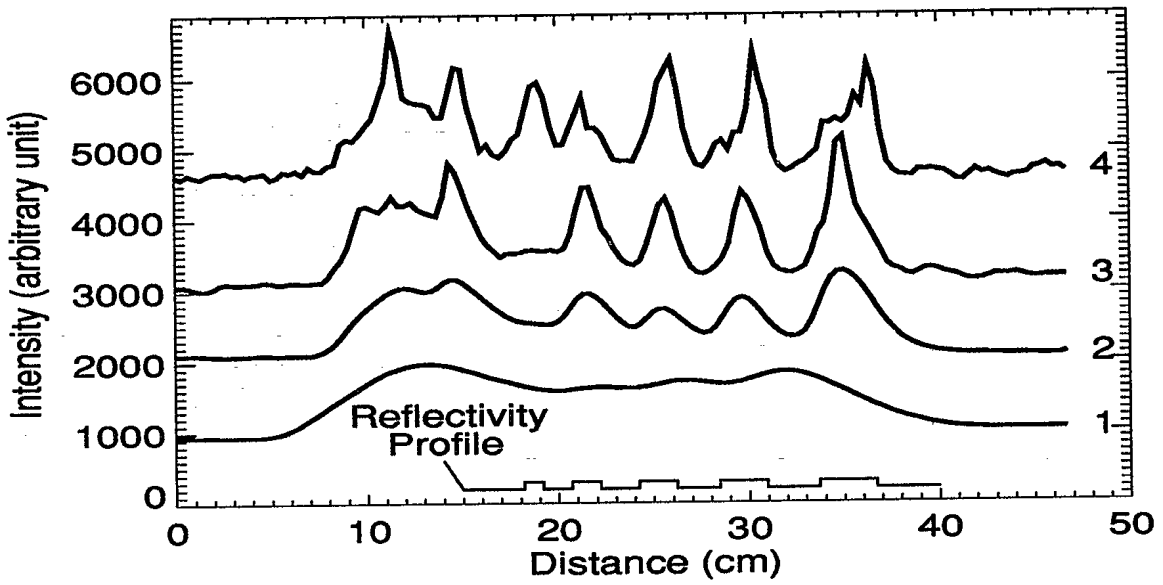

Figure 4.1

Intensity profile of a resolution target. The resolution is given for the x direction. The time constant ($\tau_{1/2}$) used for each profile is 1 ms. The scanning speeds were reduced with increasing curve index. The corresponding travelled resolution distance of the laser spot at target during the integration time ($2\times SS\times\tau_{1/2}$) was: 1-4 cm, 2-1.33 cm, 3-0.4 cm, 4-0.13 cm.

larger than that expected theoretically. However, this can be easily explained by the optical arrangement used. Optical distortion is created when a Gaussian beam is partially stopped by an aperture smaller than its diameter (possibly a beam splitter or the scanner mirror), or by off axis beam expansion (performed between BEM_1 and BEM_2). This problem can be resolved by reducing the number of optical components, the use of larger aperture optics and of an afocal beam expander.

There is another aspect in Figure 4.1 to which some attention should be given. A reduction of the laser spot travel during the detection integration time ($2\times SS\times\tau_{1/2}$) seems to increase the noise significantly. The fact that these curves were done under the same conditions (same area scanned, same laser power involved, same amount of electronic noise ($\tau_{1/2}$ = 1 ms)) brings the conclusion that this noise comes from the speckle effect. This interpretation is in agreement with the theoretical model associated with the speckle noise reduction by time averaging over the laser spot displacement (section 2.3). As the scan is done with a slower speed while keeping the same detection integration time (curves 1 $\rightarrow$ 4), the speckle noise increases as

because of the reduced number of samples taken. Scanned lines were separated by 2 cm which gave a poor spatial density of points to profile the intensity reflected in this direction.

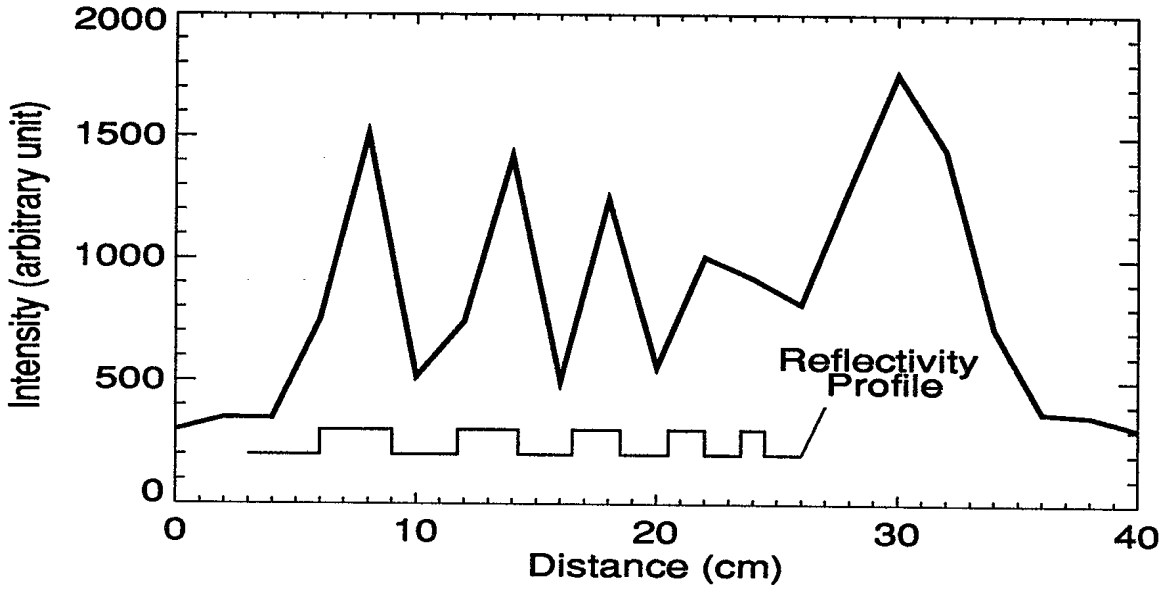

Figure 4.2

Intensity profile of the resolution target in the y direction.

a result of a smaller averaging of the reflected signal over scanned distance by the laser spot at target area. Following the theoretical model, the noise relative to the signal involved in these curves should be completely independent of the illumination power and the electronic detection configuration used. It should be only dependent on the laser spot size at target, the distance scanned during time integration, and the geometry of the optical set-up. This behavior of the imaging system is of great importance and will be studied in the laboratory.

4.2 Extrapolation Based on Experimental Results and Theoretical Model

We have observed in the previous chapter that all types of mines used in this experiment can be detected and possibly identified with adequate image processing. But an important goal of the experiments was to be able to predict the mine detection and identification capabilities for other imaging set-up configurations. To do so, the model proposed in Chapter 2 in relation with the S/N ratio observed on images produced in Chapter 3 will be analysed.

We saw in section 2.3 that the signal in an active imaging system, such as the one discussed in this document, is completely described by equation 2.20. The important unknow parameter in this equation was identified as the mine reflectivity contrast resolution ($\Delta\rho$). It is, in reality, this parameter which will fix the signal-to-noise ratio necessary to allow the detection and identification of the types of mines observed in the images. The mine reflectivity contrast is known to be strongly dependent on background, type of mine and imaging angle of view. However, from the results presented in this document, the signal-to-noise ratio involved in the present imaging system was sufficient to discern the reflectivity contrast and allow detection and identification of the mines used here on soil and prairie grass background for angles of view covering $\pm 10°$. The following expression can thus be identified.

$$\frac{P_L\, t_{L-TA}\, t_A^2\, t_{TA-D}\, \frac{A_{AS}}{d^2_{AS-TA}}\, \eta}{6 \times (NEP)\sqrt{\Delta f}} \tag{4.1}$$

which is deduced from the relation 2.20 and modified for small signal situations with the contrast reflectivity omitted. A factor 6 is used in the denominator to take in account the excess noise observed experimentally.

This expression is completely defined by the experimental configuration involved in this experiment and represents the necessary detection coefficient which will produce a S/N ratio sufficient to detect the types of mine on soil or prairie grass background ($\Delta\rho$) observed in this experiment. By evaluating the constant number corresponding to this expression for the imaging configuration set-up used in this experiment (1160 using the list of symbols), an increase or decrease of detection capability can be anticipated by comparing this constant to the one obtained with the same expression evaluated for another imaging system configuration.

From equation 4.1, four sensitive parameters are identified for consideration in a modified active imaging configuration: P_L the laser power, A_{AS} the area of the aperture stop, d_{AS-TA} the distance from collecting lens to target area and Δf the information bandwidth. These parameters are usually the ones which could present the greatest change in a different imaging system. However, the NEP of the detector can also be reduced. This detector characteristic is proportional to the dimension of

the detector. So, the detector noise can be reduced by reducing its size. However, to keep the signal at its level, a careful design could require a larger collecting lens to reduce its imaging diffraction limit to a dimension smaller than that of the detector.

4.2.1 Speckle Noise Level Estimation

It was mentioned in section 2.3 that speckle noise is proportional to the signal ($N_{spe} \propto S$). This implies that this type of noise is less critical for detection purposes. The image of the object to be detected with an active imaging system having a speckled texture will not inhibit its detection in most cases. However, the speckle noise problem is more severe when identification is attempted. In this case, a good intensity profile of the object to be identified with multiple pixels is necessary to obtain the contour of the object and potential useful details on its surface. A strong fluctuation in intensity between pixels on the object caused by speckle noise can degrade dramatically the characterization of its profile and hide surface details. On the other hand, increasing the travelled distance of the laser spot during integration time ($\tau_{1/2} \times SS \nearrow$) to reduce the speckle noise by temporal integration (see section 2.3.4) contributes also to reduce the resolution of the imaging system (see equation 2.2). A choice between a high spatial resolution or high $(S/N)_{spe}$ has to be customized according to the main function of the imaging system. A good universal solution is to adjust, if possible, the speckle noise reduction to have

$$(S/N)_{electronic} \simeq (S/N)_{speckle}$$

To be able to make this choice, an accurate model describing the speckle noise reduction by temporal integration is required. This model will be developed, verified and presented in a future report.

5. Conclusions

The capabilities of an Active Infrared Imaging Systems for minefield detection have been described. It has been demonstrated, with the conditions involved in this experiment, that the surface-laid mines used here (TMN-46, PM-60, TMB-D, and PMN-6, OZM-3, and PFM-1) on soil and prairie grass background can be detected using Active Imaging. We analysed completely this imaging system in order to extrapolate the resolution, detection, and identification capabilities obtained with this experimental set-up to other similar systems having different configurations. A constant parameter is established from which other active imaging set-ups can be compared. This comparison will give a good evaluation of the mine detection and identification capabilities of the projected set-up in comparison to the results presented in this document.

The speckle noise problem had been approached and discussed. Experimental observation of its presence has been demonstrated. The effect of the speckle noise on the signal-to-noise ratio of an active image achieved with a scanning process, and its dependence on the resolving power of the imaging system, will be studied, characterized and verified experimentally in the near future.

6. References

[1] G. C. Stuart. Infrared reflectance measurements of replica mines and reference targets (U). DRES Memorandum 1264, Defence Research Establishment Suffield, February 1989 UNCLASSIFIED.

[2] JR. Richard D. Hudson. *Infrared System Engineering.* John Wiley & Sons, New York/London/Sydney/London, first edition, 1969.

[3] W.G. Driscoll and W. Vaughan. *Handbook of Optics.* Mcgraw-Hill book Compagny, New York, first edition, 1978.

[4] J. W. Goodman. Some fundamental properties of speckle. *J. Opt. Soc. Am.*, 66(11):546–550, November 1976.

[5] J.C.Dainty. *Laser Speckle and Related Phenomena*, volume 9 of *Topics in Applied Physics*, chapter 2, pages 9–75. Springer-Verlag, Berlin/Heidelberg/New York/Tokyo, second edition, 1984.

[6] J.C.Dainty. *Laser Speckle and Related Phenomena*, volume 9 of *Topics in Applied Physics*, chapter 4.3, pages 132–143. Springer-Verlag, Berlin/Heidelberg/New York/Tokyo, second edition, 1984.

[7] T.S. McKechnie. Reduction of speckle by a moving aperture-first order statistics. *Optics Communications*, 13(1):35, January 1975.

[8] T.S. McKechnie. Reduction of speckle in a image by a moving aperture-second order statistics. *Optics Communications*, 13(1):29, January 1975.

[9] T.S.McKechnie. Measurement of some second order statistical properties of speckle. *OPTIK*, 39(3):258–267, 1974.

[10] H.Kogelnik and T.Li. Laser beams and resonators. *Applied Optics*, 5(10):1550, October 1966.

[11] V. J. Fowler. Laser scanning techniques. In *SPIE Vol.53:Laser Recording and information Handling technology*, pages 30–43, 1974.

Appendix A
Gaussian Beam Propagation Theory

A Gaussian beam is a monochromatic light wave having a circular symmetry with respect to its propagation axis and a radial amplitude distribution ($|E(r)|$) given by:

$$| E(r) | = | E_o | e^{-\frac{r^2}{\omega^2}} \tag{A.1}$$

where r is the distance from the symmetry axis and ω represents the distance from the central axis where the amplitude falls to 37 % of its maximum $|E_o|$. This particular amplitude distribution represents the most important family of solutions to the wave equation in a laser cavity [10]. It will describe the field built-up distribution in the amplification medium of the laser and along its propagation axis. From equation A.1, the radial intensity distribution can be defined as

$$I(r) = | E(r) |^2 = | E_o |^2 e^{-\frac{2r^2}{\omega^2}} \tag{A.2}$$

Using the radial symmetry of this intensity and the definition of the total power P for a Gaussian beam, the following relation is derived:

$$I(r) = \frac{2P}{\pi\omega^2} e^{-\frac{2r^2}{\omega^2}} \tag{A.3}$$

It is possible then, when P and ω are known, to describe completely the Gaussian beam intensity distribution across its section. A useful relation which can be deduced from this definition is the power surrounded by an aperture of radius a:

$$P(a) = P\left[1 - e^{-\frac{2a^2}{\omega^2}}\right] \tag{A.4}$$

This formula is shown graphically in Figure A.1. This relation can be very helpful to evaluate how a particular aperture in an optical set-up disturbs the Gaussian beam.

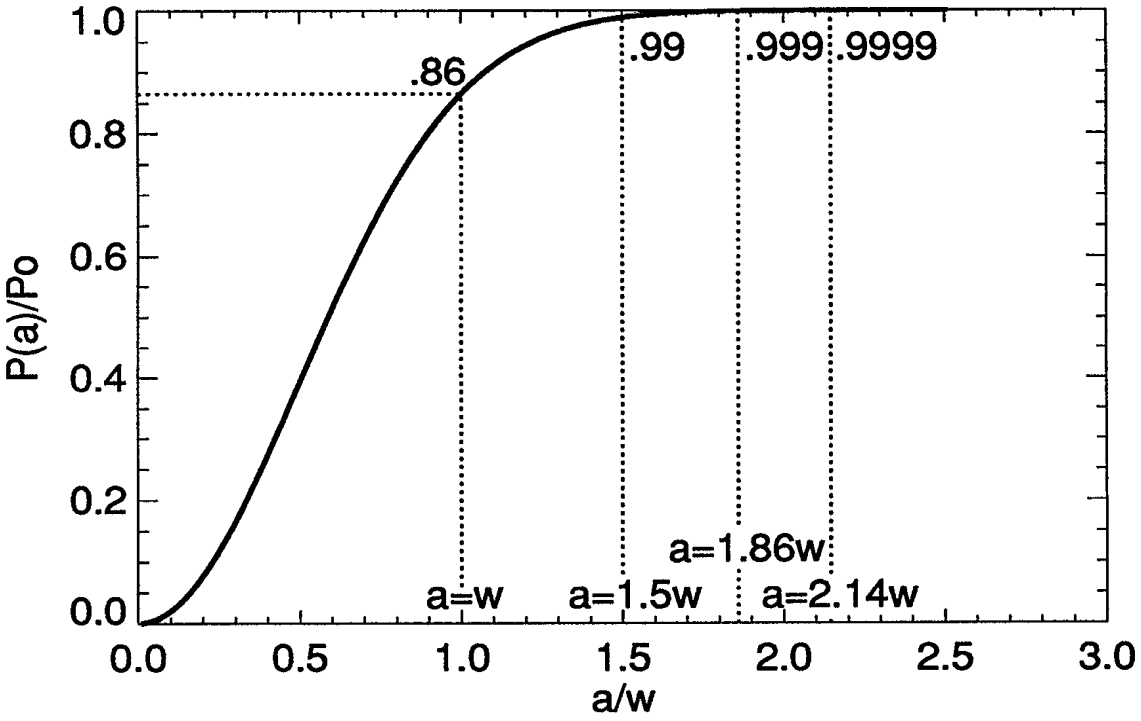

Figure A.1

Power inside an aperture of radius a. w is the radius of the Gaussian beam at $1/e^2$ of its maximum intensity.

When a more complete solution of the wave equation is derived for the Gaussian beam family [10], another important characteristic appears. This characteristic is the lateral dispersion of the Gaussian profile with its propagation. This lateral dispersion is described by the dependence of ω with z , the propagation axis. The equation defining this relation is the following:

$$\omega^2(z) = \omega_o^2 \left[1 + \left(\frac{\lambda(z - z_o)}{\pi\omega_o^2}\right)^2\right] \tag{A.5}$$

By defining ϕ as the diameter of the Gaussian beam ($\phi = 2\omega$), equation A.5 takes the following form:

$$\phi^2(z) = \left[\phi_o^2 + \left(\frac{4\lambda(z - z_o)}{\pi\phi_o}\right)^2\right] \tag{A.6}$$

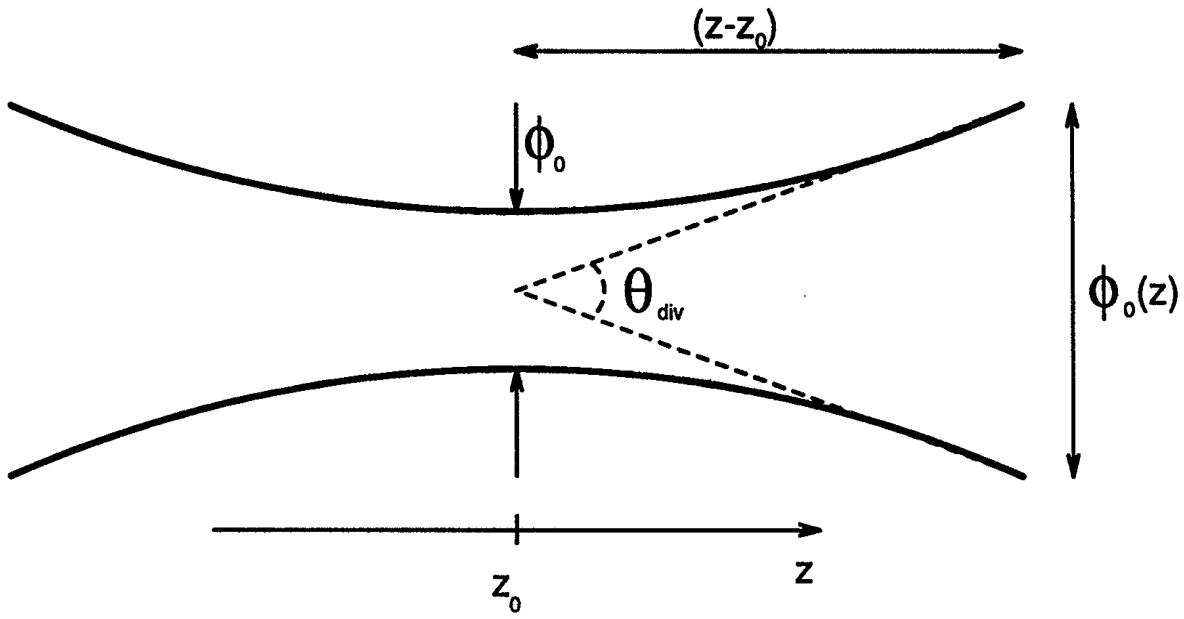

Figure A.2

Schematic geometry of a Gaussian beam propagation.

where

λ	light wavelength of the Gaussian beam.
ω	distance from the central axis where the intensity falls to $1/e^2$ of its maximum.
ω_o	minimum ω.
ϕ	distance equal to $2 \times \omega$, referred as the beam diameter.
ϕ_o	minimum ϕ .
z	coordinate along the propagation axis of the Gaussian beam.
z_o	position where the diameter of the Gaussian beam is minimum.

In this last definition, ϕ represents the diameter of a Gaussian beam at $1/e^2$ (14%) of its intensity. From this relation, a change in diameter of a Gaussian beam with its propagation axis is completely defined if its minimum beam diameter (ϕ_o) and the position of this minimum (z_o) are known. This last equation (A.6) can be approximated by

$$\phi(z) = \frac{4\lambda(z - z_o)}{\pi\phi_o} \tag{A.7}$$

when z is large compared to ϕ_o. From this last equation, the definition of the beam divergence (θ_{div}) is established.

$$\theta_{div} = 2\arctan\left(\frac{\phi(z)}{2(z - z_o)}\right) \simeq \frac{4\lambda}{\pi\phi_o} \tag{A.8}$$

This characteristic, the beam divergence, is a basic property for most lasers and it is given by the manufacturer. However, with the use of optics like beam expanders, ϕ_o and z_o can be modified and adjusted to a needed configuration.

Appendix B
Scanning Resolution Theory

In a scanning system where the initial beam diameter (ϕ_1) and the distance between the position of this initial beam diameter and the target area is fixed, it is possible to develop a complete model from which the maximum scanning resolution can be deduced [11]. In this model, the scan resolution (N) is defined as the ratio between the total scanned angle ($\Delta\varphi$) and the illumination resolution angle (θ_{res}).

$$\mathrm{N} = \frac{\Delta\varphi}{\theta_{res}} \tag{B.1}$$

For purposes of simplification, the following model is established for a circularly scanned screen (see Figure B.1). In this case, the scan resolution can also be rewritten as

$$\mathrm{N} = \frac{\mathrm{R}\Delta\varphi}{\phi_2} \tag{B.2}$$

Using the parameters definition in the list of symbols and equation A.6, equation B.2 can be rewritten as

$$\mathrm{N} = \frac{(z + z_1)\Delta\varphi}{\left[\phi_\circ^2 + \left(\frac{4\lambda z}{\pi\phi_\circ}\right)\right]^{1/2}} \tag{B.3}$$

Now, to evaluate the optimum scan resolution (N) possible for an optical set-up, N is differentiated with respect to the variable z and the optimum distance z_{opt} is evaluated. The result is as follows:

$$z_{opt} = \left(\frac{\pi\phi_\circ^2}{4\lambda}\right) / z_1 \tag{B.4}$$

Thus, for a set-up where z_1 and $\phi_\circ$ are fixed, z_{opt} is the optimum distance from the minimum beam diameter position to place the projection screen to obtain a maximum

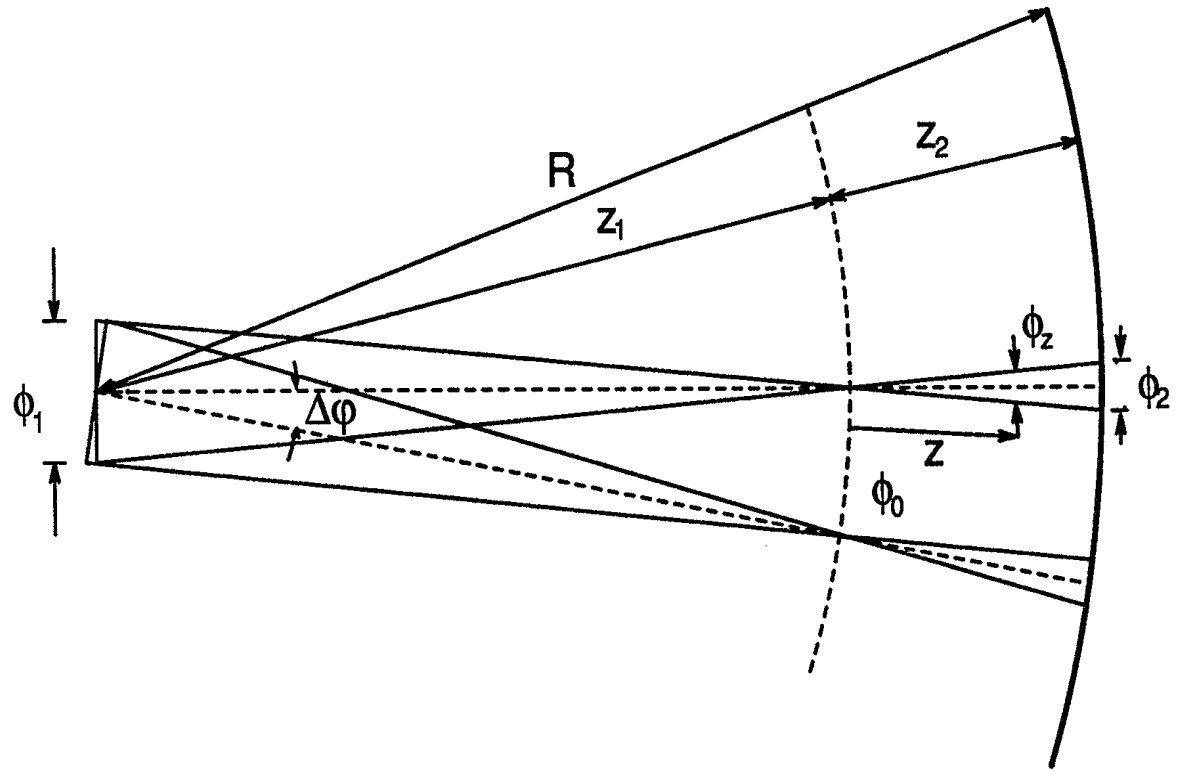

Figure B.1

Deflection of a convergent laser beam. The symbols are described in the list of symbols.

scan resolution (N_{max}). By replacing the definition of z_{opt} (equation B.4) in the scan resolution definition in equation B.3, we obtain

$$N_{max} = \left(\frac{\pi}{4}\right) \Delta\varphi \left(\frac{\phi_1}{\lambda}\right) \tag{B.5}$$

An important property of this relation is its optical invariance. Indeed, if the collimated beam is passed through an angle magnifying telescope after the scanner, the initial beam diameter (ϕ_o) will be demagnified by the same factor as the magnification applied to the total scanned angle ($\Delta\varphi$), keeping the product $\Delta\varphi\,\phi_1$ invariant. It is possible to demonstrate that N_{max} does not depend of any optics placed after the scanner.

Using the definition of the beam divergence (θ_{div}) in relation A.8 where ϕ_1 is substituted by ϕ_o, N_{max} can be rewritten as

$$N_{max} = \frac{\Delta\varphi}{\theta_{div}} \tag{B.6}$$

This expression is the simplest definition of the maximum possible resolution possible. To make this last result more useful and easier to manipulate when an optical scanning system is analysed, relations B.3, B.4, and B.5 can be transformed by cross substitution to obtain expressions for z_1, z_2, and ϕ_o

$$z_1 = \frac{R}{\left[1 + \left(\frac{4\lambda R}{\pi \phi_1^2}\right)^2\right]} \tag{B.7}$$

$$z_2 = R - z_1 \tag{B.8}$$

$$\phi_o = \frac{\phi_1}{\left[1 + \left(\frac{\pi \phi_1^2}{4\lambda R}\right)\right]^{1/2}} \tag{B.9}$$

The minimum spot size at the screen (ϕ_{min}) is extracted from the substitution of equation B.6 in relation B.2:

$$\phi_{min} = \frac{4\lambda R}{\pi \phi_1} \tag{B.10}$$

This last relation expresses the smallest beam spot size feasible at distance R between the projection screen and the origin beam position with an initial beam diameter ϕ_1.

Appendix C
Sunlight Illumination Analysis

An important question to answer in active IR imaging system of the ground is what part of the infrared radiation coming from the ground is due to sunlight reflection at 10.6 μm. To evaluate this effect, we will consider the atmosphere transparent at this wavelength and the sun as a perfect blackbody. Using the blackbody spectral distribution radiation relation shown in section 2.3 (equation 2.16), we evaluate the spectral irradiation of the sun as

$$\mathrm{M}_{\lambda}^{\mathrm{sun}}(10.6\mu\mathrm{m}) = 1 \times 10^{10} \left(\frac{\mathrm{W}}{\mathrm{m}^3}\right) \tag{C.1}$$

To obtain this value, the sun temperature given in Table VIII is used. This radiation will travel the sun-earth distance before to be reflected by the soil. To characterize this situation, the spectral intensity generated by the sun at earth level is evaluated using the inverse square law of propagating radiation.

$$\mathrm{I}_{\lambda}^{\mathrm{sun}}(10.6\mu\mathrm{m}) = \frac{\mathrm{M}_{\lambda}^{\mathrm{sun}}}{d_{s-e}^2}\left(\pi\left(\frac{\phi_{\mathrm{sun}}}{2}\right)^2\right) \tag{C.2}$$

With the parameters of Table VIII, the incident intensity of the sun at earth level and at 10.6 μm in a spectral bandwidth of 0.35 μm as the filter specification used in this experiment is

$$\mathrm{I}_{0.35}^{\mathrm{sun}}(10.6\mu\mathrm{m}) = 59 \left(\frac{\mathrm{mW}}{\mathrm{m}^2}\right) \tag{C.3}$$

Comparing this intensity to the equivalent one created by the laser illumination ($< \mathrm{I}_{laser} > \simeq \frac{400\,\mathrm{mW}}{\pi(\phi_{1/e^2}/2)^2\,\mathrm{m}^2} = 1000\ \mathrm{W/m^2}$), the sun illumination for this experiment configuration can be assumed to be negligible.

Table VIII

Solar Characteristics.

Sun Surface Temperature	5900°K
Sun Diameter (ϕ_{sun})	6.95×10^8 m
Distance Sun-Earth (d_{s-e})	150×10^9 m

Appendix D
Photographs of the Mines Used in this Study

In this appendix, photographs of the six different mines used in this study are shown. Their name, the mine type (anti-tank or anti-personnel), and the construction material are specified. For more information, the reader can consult [1].

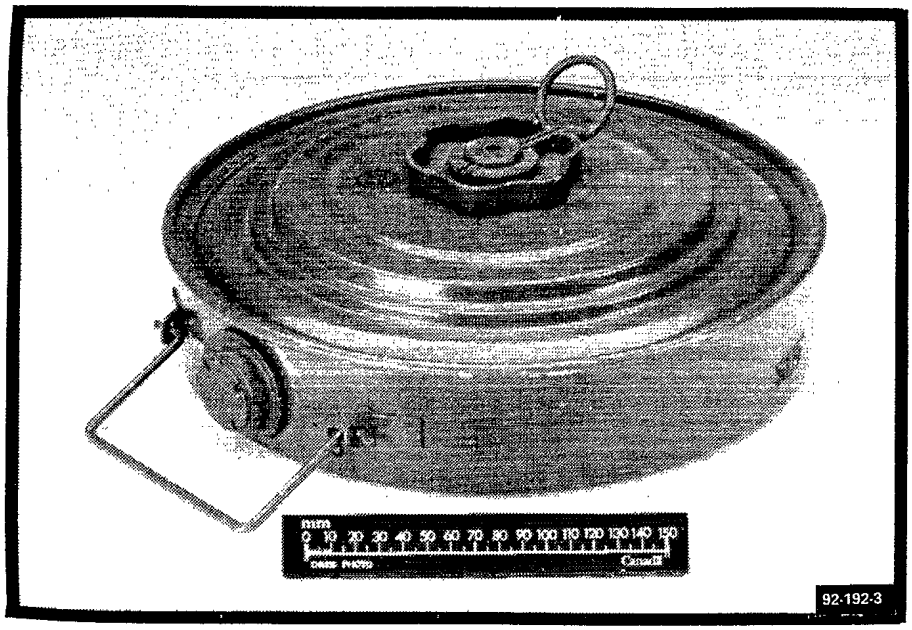

Figure D.1

TMN-46 anti-tank mine. Construction material: metal. Origin: Russian.

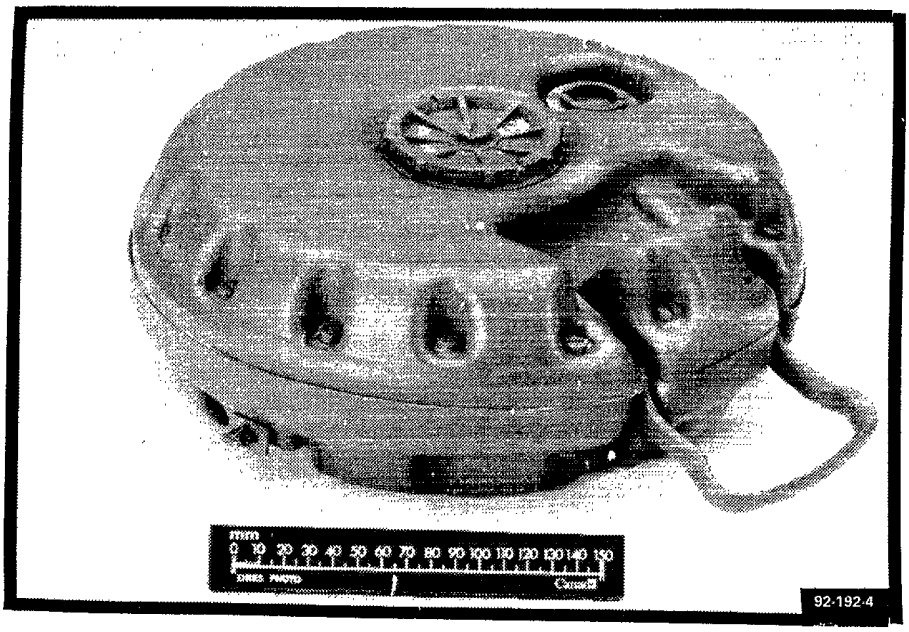

Figure D.2

PM-60 anti-tank mine. Construction material: polymeric. Origin: Russian.

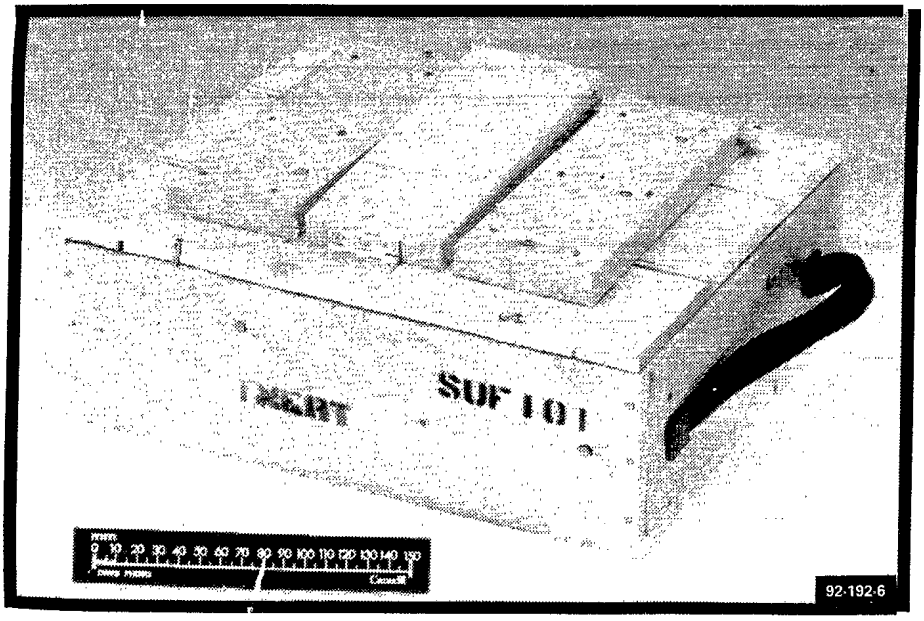

Figure D.3

TMB-D anti-tank mine. Construction material: wood. Origin: Russian.

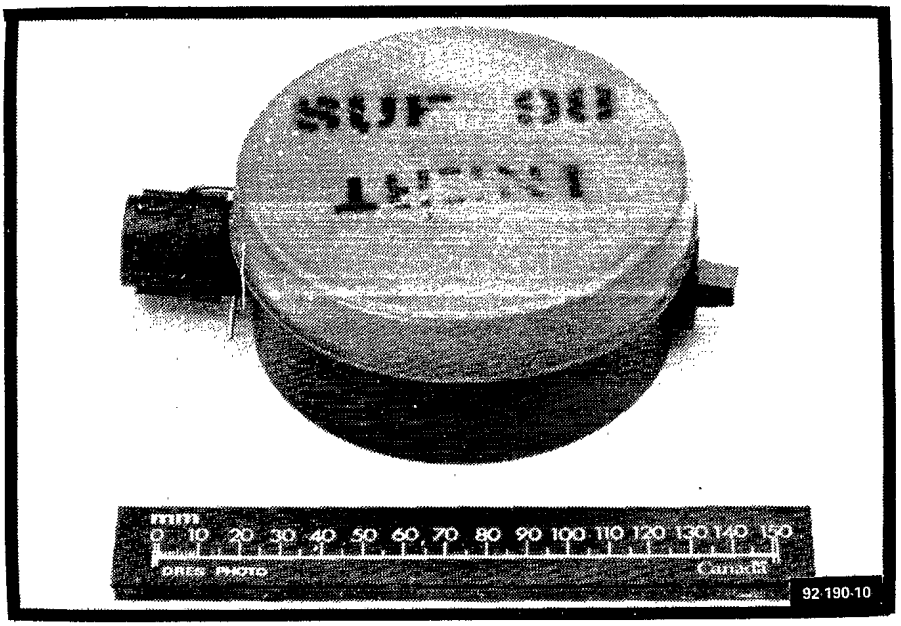

Figure D.4

PMN-6 anti-personnel mine. Construction material: polymeric. Origin: Russian.

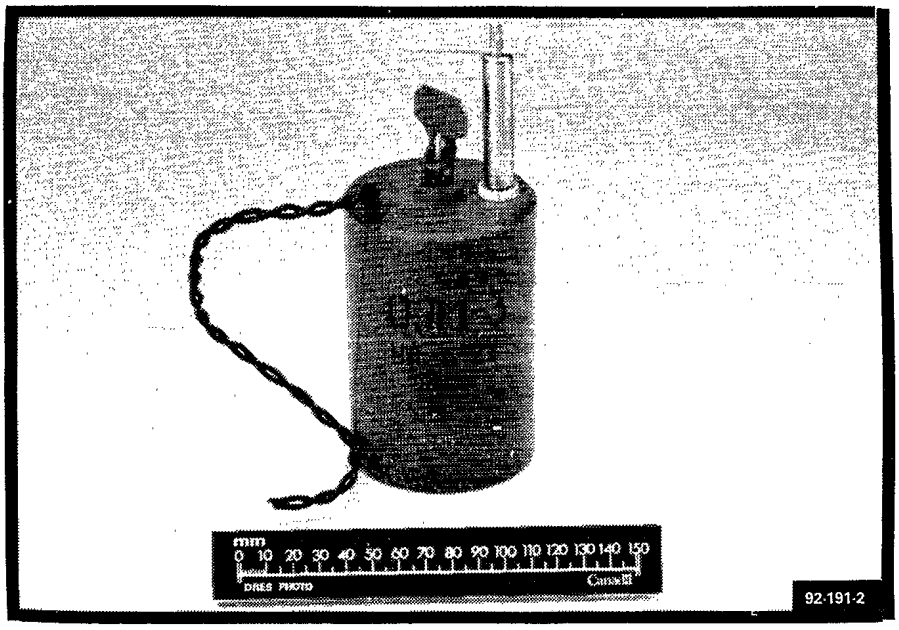

Figure D.5

OZM-3 anti-personnel mine. Construction material: metal. Origin: Russian.

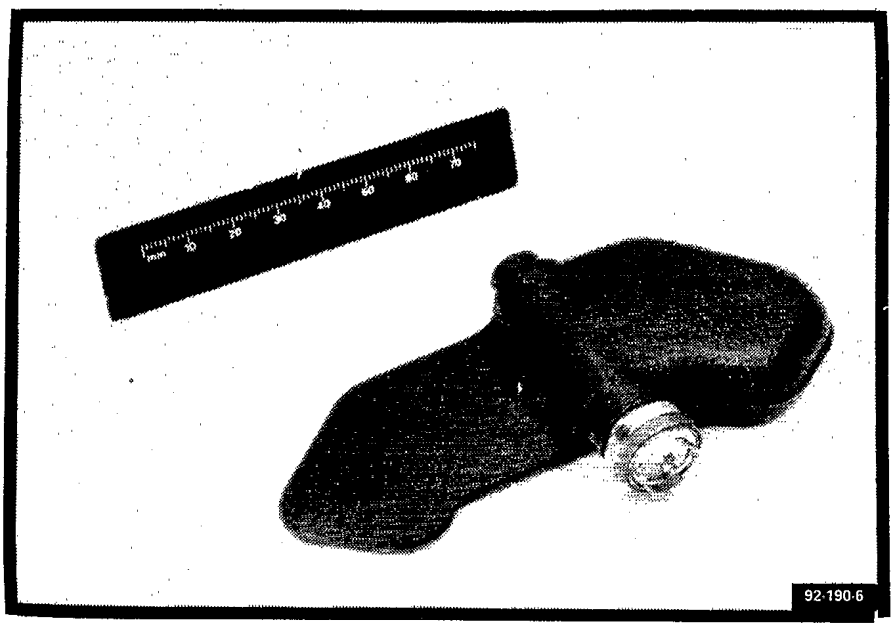

Figure D.6

PFM-1 anti-personnel mine. Construction material: polymeric. Origin: Russian.

DOCUMENT CONTROL DATA

(Security classification of title, body of abstract and indexing annotation must be entered when the overall document is classified)

1. ORIGINATOR (the name and address of the organization preparing the document. Organizations for whom the document was prepared, e.g. Establishment sponsoring a contractor's report, or tasking agency, are entered in section 8.)

DRES, Ralston, Alberta, T0J 2N0

2. SECURITY CLASSIFICATION (overall security classification of the document. including special warning terms if applicable)

Unclassified

3. TITLE (the complete document title as indicated on the title page. Its classification should be indicated by the appropriate abbreviation (S,C,R or U) in parentheses after the title.)

Analysis and Trial of an Active Longwave Infrared Imaging System for Minefield Detection and Identification.

4. AUTHORS (Last name, first name, middle initial. If military, show rank, e.g. Doe, Maj. John E.)

Simard, Jean-R

5. DATE OF PUBLICATION (month and year of publication of document)

November 1992

6a. NO. OF PAGES (total containing information. Include Annexes, Appendices, etc.)

82

6b. NO. OF REFS (total cited in document)

11

6. DESCRIPTIVE NOTES (the category of the document, e.g. technical report, technical note or memorandum. If appropriate, enter the type of report, e.g. interim, progress, summary, annual or final. Give the inclusive dates when a specific reporting period is covered.)

Suffield Report

8. SPONSORING ACTIVITY (the name of the department project office or laboratory sponsoring the research and development. Include the address.)

9a. PROJECT OR GRANT NO. (if appropriate, the applicable research and development project or grant number under which the document was written. Please specify whether project or grant)

9b. CONTRACT NO. (if appropriate, the applicable number under which the document was written)

10a. ORIGINATOR'S DOCUMENT NUMBER (the official document number by which the document is identified by the originating activity. This number must be unique to this document.)

10b. OTHER DOCUMENT NOS. (Any other numbers which may be assigned this document either by the originator or by the sponsor)

11. DOCUMENT AVAILABILITY (any limitations on further dissemination of the document, other than those imposed by security classification)

(X) Unlimited distribution
( ) Distribution limited to defence departments and defence contractors; further distribution only as approved
( ) Distribution limited to defence departments and Canadian defence contractors; further distribution only as approved
( ) Distribution limited to government departments and agencies; further distribution only as approved
( ) Distribution limited to defence departments; further distribution only as approved
( ) Other (please specify):

12. DOCUMENT ANNOUNCEMENT (any limitation to the bibliographic announcement of this document. This will normally correspond to the Document Availabilty (11). However, where further distribution (beyond the audience specified in 11) is possible, a wider announcement audience may be selected.)

Unlimited

13. ABSTRACT (a brief and factual summary of the document. It may also appear elsewhere in the body of the document itself. It is highly desirable that the abstract of classified documents be unclassified. Each paragraph of the abstract shall begin with an indication of the security classification of the information in the paragraph (unless the document itself is unclassified) represented as (S), (C), (R), or (U). It is not necessary to include here abstracts in both offical languages unless the text is bilingual).

This document shows theoretical and experimental results of the capabilities of an active longwave infrared imaging system on surface-laid minefields. Three anti-tank and three anti-personnel mines on soil and prairie grass backgrounds are investigated for the detection and identification capabilities of this scanning imaging system. After establishing the detection and identification capabilities of the set-up used in this experiment, an associated parameter of the imaging system is evaluated which can be used to estimate the detection and identification capabilities of other imaging set-ups with different configurations. In addition, speckle is studied and its presence is demonstrated in the images obtained.

14. KEYWORDS, DESCRIPTORS or IDENTIFIERS (technically meaningful terms or short phrases that characterize a document and could be helpful in cataloguing the document. They should be selected so that no security classification is required. Identifiers, such as equipment model designation, trade name, military project code name, geographic location may also be included. If possible keywords should be selected from a published thesaurus. e.g. Thesaurus of Engineering and Scientific Terms (TEST) and that thesaurus-identified. If it is not possible to select indexing terms which are Unclassified, the classification of each should be indicated as with the title.)

Minefield Detection
Carbon Dioxide
Laser
Speckle
Active Imaging
CO_2
lR

93-00043
127305